Journal of Energy Storage 58 (2023) 106284

Contents lists available at ScienceDirect

Journal of Energy Storage

journal homepage: www.elsevier.com/locate/est

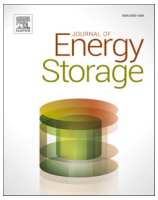

Research papers

The influence of the metal foam layer shape on the thermal charging response time of a latent heat thermal energy storage system

Mehdi A. Fteiti [a], Mohammad Ghalambaz [b,*], Obai Younis [c,d], Mikhail Sheremet [b], Muneer Ismael [e]

[a] Physics Department, Faculty of Applied Sciences, Umm Al-Qura University, Makkah 24381, Saudi Arabia
[b] Laboratory on Convective Heat and Mass Transfer, Tomsk State University, 634045 Tomsk, Russia
[c] Department of Mechanical Engineering, College of Engineering in Wadi Addwasir, Prince Sattam Bin Abdulaziz University, Saudi Arabia
[d] Department of Mechanical Engineering, Faculty of Engineering, University of Khartoum, Khartoum 11111, Sudan
[e] Mechanical Engineering Department, College of Engineering, University of Basrah, Basrah, Iraq

ARTICLE INFO

Keywords:
Metal foam
Phase change materials
Metal foam layer shape
Thermal charging time

ABSTRACT

In the current study, the impact of various foam shapes and configurations was addressed for the first time on the thermal energy storage rate. A partial layer of metal foam was used to improve the heat transfer rate in a channel-shaped latent heat thermal energy storage unit for solar thermal energy storage. The channel was heated at the right vertical wall while half of the channel was filled with a layer of metal foam. The enthalpy porosity model was utilized for simulating the melting heat transfer in the channel. The finite element method was employed to solve the governing equations. Several design configurations for the placement of the metal foam layer were examined. The findings showed that placing the metal foam layer in an L shape form along the left and bottom walls could yield maximum thermal energy storage power (0.57 kW). Diagonal placement of the porous layer along the right and bottom walls gives the lowest thermal energy storage power (0.23 kW). Therefore, changing the shape of the metal foam layer could alter the storage power by about 60 % for a fixed amount of metal foam. Therefore, the shape of the metal foam layer is an important design parameter that should be selected carefully.

1. Introduction

Due to recent technological advancements and modern living demands, the world's energy consumption is expected to double every two decades [1]. Worldwide, countries are becoming increasingly concerned about global warming and the resulting climate change [2]. Using renewable energy provides an opportunity to develop more efficient and eco-friendly forms of energy. An energy source such as this is periodic, variable, and unpredictable at any particular location. It results in a mismatch between the supply and demand for energy [3]. Through thermal energy storage (TES), energy storage can close the gap between energy demand and supply [4]. The three basic kinds of TES are latent heat storage (LHTES), storage of sensible heat, and storage of thermochemical energy [5].

The sustainable LHTES technique can use the extra thermal energy released into the environment by renewable energy sources, making it extensively applicable in various practical applications (e.g., industrial waste heat recovery, electronic cooling, and solar energy systems) [6]. Phase change materials (PCM) have recently attracted considerable attention in LHTES. PCMs are desirable for various reasons, including repeatable phase transition, non-toxicity, non-corrosive properties, high latent heat of fusion per unit volume, a melting point within acceptable operating temperatures, and a modest volume change during phase transformation [7]. However, its low thermal conductivity is a significant barrier to its use in several types of thermal appliances. PCM-based devices must have efficient thermal conductivity to store and release energy uniformly and quickly. It has been suggested to boost the rate of heat transfer in many different ways, including the use of nanoparticles [8], fins [9,10], heat pipes [11], and porous matrix structures [12]. Thermal energy storage enclosures can be produced in different enclosure shapes, including shell-tube shapes [13,14].

Metal foams (MF), as an example of a porous matrix structure,

* Corresponding author.
E-mail addresses: mafteiti@uqu.edu.sa (M.A. Fteiti), m.ghalambaz@gmail.com (M. Ghalambaz), oubeytaha@hotmail.com (O. Younis), sheremet@math.tsu.ru (M. Sheremet), muneer.ismael@uobasrah.edu.iq (M. Ismael).

https://doi.org/10.1016/j.est.2022.106284
Received 19 May 2022; Received in revised form 3 October 2022; Accepted 26 November 2022
Available online 14 December 2022
2352-152X/

enhance melting heat transfer. An absorbent structure is an MF, and the filling material is a PCM. Tauseef et al. [15] examined the usage of porous materials to enhance heat rate in PCM. Yu et al. [16] demonstrated that the size of the MF and the porosity significantly affect its solidification rate. Joshi and Rathod [17] numerically investigated the heat transfer performance of several MF porosities and filling height ratios in a two-dimensional square cavity. They observed that MF only increased heat transport in the bottom section and that when the filling height ratio or porosity decreased, so did the total melting time.

Gaedtke et al. [18] used the lattice Boltzmann technique to predict the pore size of MF impregnated with PCM. The surface area of MF significantly influenced the melting rate. Ali [19] investigated the increased heat transfer of PCM induced by the interactions of PCM with porous media in a heatsink. Based on the results, the metal foam improves the heat transfer rate but reduces the durability of heatsink cooling. Li et al. [20] studied three distinct techniques for enhancing a triple-tube LHTES, including the addition of MF, the addition of nanoparticles, and geometry modification. The findings indicated that when both nanoparticles and porous media were used, the latter's influence on performance was insignificant. The entire solidification process can be sped up with metal foams with a lower porosity or nanoparticles with a higher volume fraction. Meng et al. [21] used a two-dimensional numerical model to evaluate the influence of foamed copper porosity. The findings reveal that reducing the porosity improves the thermal characteristics of the PCM, notably between 92 and 98 %. Still, it reduces the heat storage capacity of the PCM by roughly 22.3 kJ for every 2 % drop in porosity. Guo et al. [22] utilized a compressed MF to enhance heat transfer and reduce the melting time. The foam compression reduced the melting time by 13.9 %. However, an over-compression of the MF could increase the melting time and impose foam non-uniformity.

Among the recently invented battery modules for electric vehicles is one that utilizes MFPCM to regulate temperature [23]. MFPCM is used in conjunction with an arrangement / cooling circuit of two opposing fluid currents to maintain an acceptable temperature range for the battery module. A combination of electronic equipment and a heat abstractor also is introduced in innovation to increase the chip's radiating efficiency while simultaneously lowering the shell temperature of the electronic equipment [24]. The drain pan, PCM layer, and MF heat-conducting layer are all included in this utility heat abstractor idea. Using pore-scale models of primitive cell types to form foam structures, Qureshi et al. [25,26] attempted to improve conduction using PCM infiltrated MF. Based on their findings, the melt duration of PCM can be reduced by up to 30 % compared to pure PCM. A multi-objective Pareto optimization was carried out using a genetic algorithm to analyze the overall process time of a finned heat sink made of PCM and MF by Bianco et al. [27]. With various constant temperature heater sites, Sardarari et al. [28] analyzed the average temperature as well as the average PCM liquid percentage over time for a porous-PCM system. By shifting the heater from the bottom to the sidewall and top, melting time was reduced by 70.5 % and 4.7 %, respectively.

Zi-Qin et al. [29] addressed the thermal behavior of a heatsink partially filled by a metal foam layer. They examined the impact of foam layer height (foam/clear space ratio). The results showed that increasing the foam height can gradually raise the heat transfer rate. However, the performance raise was found to become saturated as the MF height reached the top. Thus, the authors concluded filling 2/3 of the heatsink by MF could be more practical compared to fully filling the heatsink by MF. Xu et al. [30] simulated the melting heat transfer in a horizontally mounted shell-tube shape enclosure. The PCM was heated from the tube, and the shell was insulated. The aim was to optimize the amount of MF for the best melting (thermal charging) performance. The authors concluded placing the foam layer at the bottom is more beneficial since natural convection can heat the top region effectively. Moreover, filling a portion of the enclosure (0.7 height from bottom) is cost effective and can result in 3 % improvement in thermal energy storage rate density and 28 % saving in MF compared to an enclosure fully filled by MF. In another study, Xu et al. [31] examined the impact of different configurations of MF layers on melting performance in the same geometry as [30]. The outcomes indicate a well-configured MF layer can save the melting time by 80 % compared to a case with no MF.

Sutradhar et al. [32] developed an analytical model to assess the thermal performance of rectangular TES based on metal foam PCM (MFPCM) under transient and steady heat load conditions. Yu et al. [33] explored experimentally how the MF structure affects the MFPCM's ability to regulate temperatures. Zhuang et al. [34] investigated the heat transfer capability of a hybrid LHTES with PCM, nanoparticles, and metal foam in a cubic cavity with an internal heater. For four distinct composite PCMs, Naldi et al. [35] offered a quantitative examination of the discrepancies between experimental data and numerical conclusions produced by using the most often utilized correlations. Shakibi et al. [36] studied the role of PCMs combined with copper and aluminum foam on photovoltaic panel temperature reduction. The impacts of MF type, foam porosity, and PCM thickness on the overall performance are also investigated. One innovative design of macro encapsulated PCM has been proposed by Baruah et al. [37], in which the capsules are filled with MF structures incorporated in PCM.

Even though the above literature analysis shows that MF enhances the heat transfer performance of PCMs, each technique has some shortcomings. MFs don't participate in latent energy storage since they do not change phase and cause the natural convection flow to be suppressed. However, MF can contribute to heat transfer by sensible heat for a reasonable temperature difference. Furthermore, filling MF occupies part of the PCM volume and increases the system's weight. Some researchers attempt to optimize the placement or amount of MF layer in LHTES units. However, there is no study to address the impact of different shapes of MF layer in a channel shape LHTES unit. The present study aims to analyze the impact of the location and shape of a metal foam layer on the charging time of a channel shape LHTES unit for the first time.

2. Model description and formulation

2.1. Model description

Open metal foams are advantageous in enhancing the PCMs' thermal conductivity while allowing some degree of convective heat transfer in liquid regions of the enclosure. However, since metal foams do not contribute to thermal energy storage, they add weights/volume to a PCM enclosure. However, it should be noted that they can contribute by their sensible heat when the temperature variation is notable. Therefore, improving the heat transfer capability of thermal energy storage without compromising its storage capacity is a vital engineering goal in designing PCM thermal energy storage units.

In the current work, the PCM enclosure is made of a channel partially filled with a layer of metal foam. The weight (volume) of the metal foam layer is kept constant at 50 % volume of the enclosure. As a thermal energy storage unit application, a view of solar thermal energy storage is depicted in Fig. 1. (a). Fig. 1(b) shows a schematic view of the storage model. The heat transfer fluid (HTF) flows through the HTF channel with a hot temperature (T_h) and charges the PCM inside the channel enclosure. The PCM absorbs the HTF heat in the form of sensible and latent heat, and the phase changes to a liquid form. Fig. 1(c) depicts a 2D view of a single enclosure, which is heated by HTF. The size of the storage assembly depends on the required heat capacity of the application. The vertical or horizontal arrangement of the units also depends on the available horizontal or vertical space. Since the present design is almost independent of the unit arrangements, the capacity and storage power of units can simply add up to meet the application demands.

The current study aims to improve the PCM's melting (energy absorption) time in the unit by adding a metal foam layer. The presence of a metal layer affects the dynamic of charging PCM and the motion of the solid-liquid interface inside the PCM enclosure. Here the goal is to

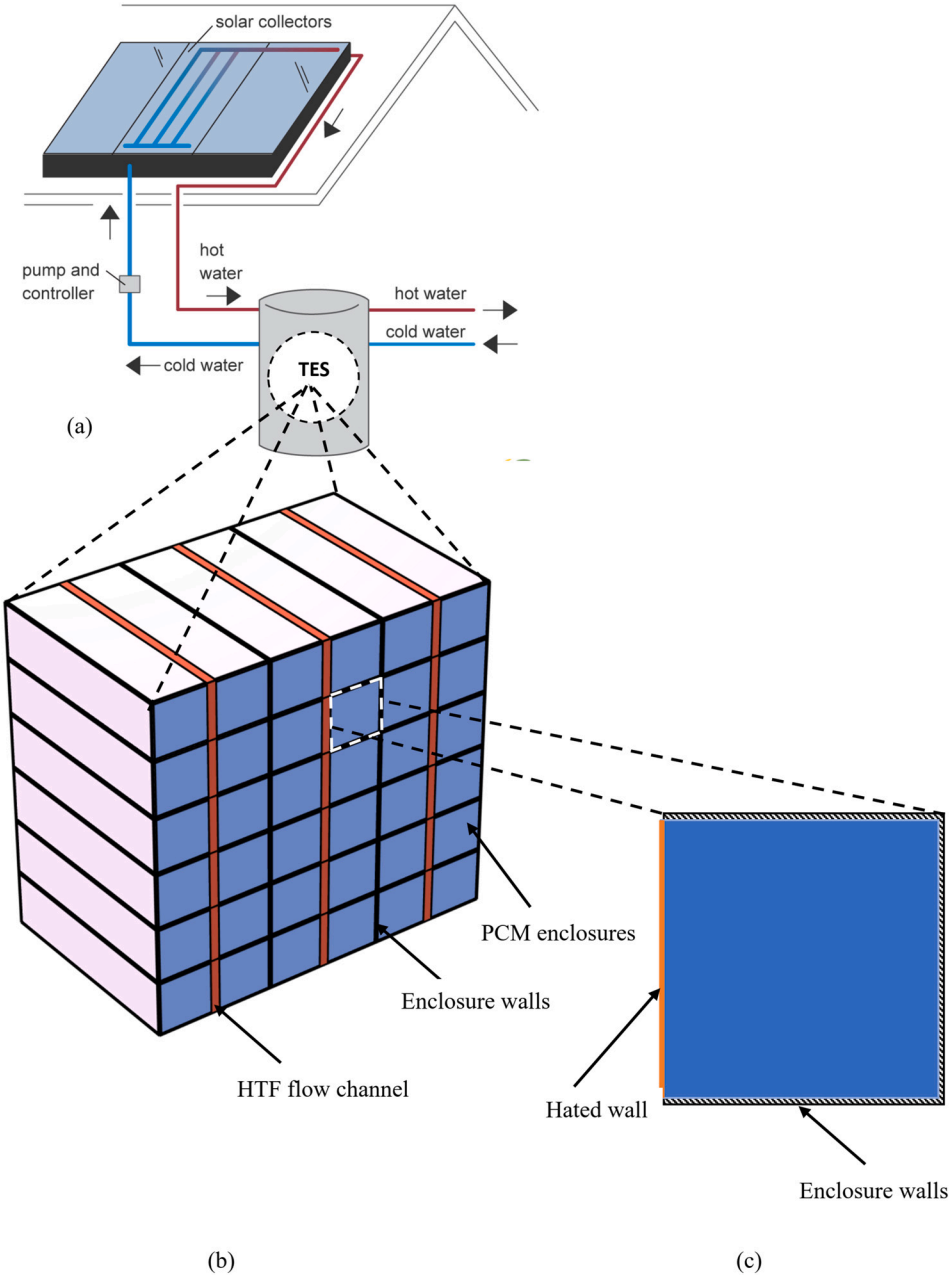

Fig. 1. Model of the TES unit; (a) A system of a solar collector with a TES unit; (b) A 3D detailed view of PCM enclosures and HTF flow direction inside a TES unit; (c) A 2D model of a PCM enclosure.

change the shape design of the metal foam layer to reach minimum charging time (full melting). In this research, twelve metal foam layer configurations were selected with the aim of enhancing the heat transfer in the PCM enclosures. Fig. 2 depicts the proposed metal foam layer configurations.

2.2. Model formulation

2.2.1. Governing equations

It is assumed the metal foam is placed in the enclosure with a preloaded pressure, and the thermal resistance between the heated surfaced and the metal foam was neglected. The metal foam is uniform with isotropic properties. The fluid flow in the porous metal foam was modeled using the Darcy-Brinkman model, while the Navier-Stocks model governs the fluid flow in the clear regions. The enthalpy porosity approach was used to model PCM's phase change heat transfer in the enclosure. The phase change occurs in a small temperature window around the fusion temperature in this approach. The liquid volume fraction changes from zero (pure solid) to unity (pure liquid). The velocity in the solid zones is forced to zero using mushy source terms.

Moreover, the local thermal equilibrium between MF and PCM was assumed. The ligaments of the porous metal foam and the PCM are at non-identical temperatures due to large variations in thermal diffusivity. Such a temperature difference can be considered using a local thermal non-equilibrium model. However, the experimental study of Agwu Nnanna [38] indicates the local thermal non-equilibrium effects only in the initial stages of the phase change. Then, the local thermal equilibrium condition reaches quickly. Jiao et al. [39] investigated the local thermal non-equilibrium effect for the paraffin/copper foam and paraffin/nickel foam using numerical and experimental approaches. They showed that the difference between the paraffin and foam temperatures was evident only near the heated boundary in the first few

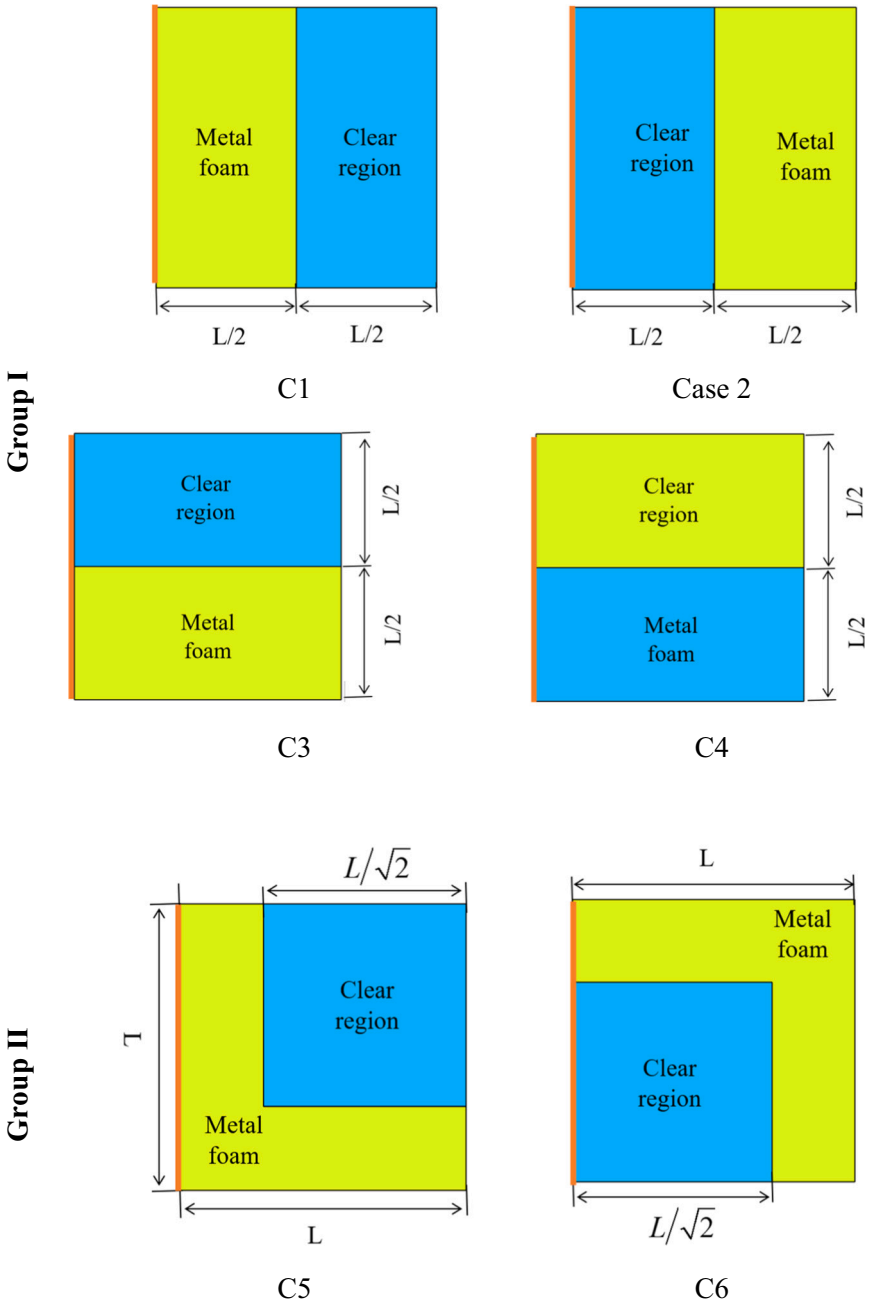

Fig. 2. Metal foam layer configuration for enhancing the charging rate (reducing melting time) in the enclosure. Group I: Straight partition; Group II: Square partition; Group III: Diagonal partition.

minutes. Pore-scale analysis of Hu and Gong [40] also shows that the non-equilibrium effects gradually weaken and then vanish as phase change advances.

Moreover, the theoretical study of Mahdi et al. [41] also confirms the difference between local thermal non-equilibrium and local thermal equilibrium models is small. The reason can be attributed to the slow motion of the melting front. Although the thermal diffusivity between the solid and PCM phase is considerable, the temperature at the phase change front is constant, and the phase change front moves slowly. Thus, a local thermal equilibrium can provide reasonably accurate results for most engineering thermal energy storage applications. Hence, a local thermal equilibrium model has been used to reduce the complexity of equations and focus on the impact of porosity distribution on thermal energy storage. The governing equations for the conservation of mass, momentum, and energy are written as follows [42]:

Conservation of mass:

$$\frac{\partial u}{\partial x}+\frac{\partial v}{\partial y}=0 \tag{1}$$

Momentum equation in x and y directions:

$$\frac{\rho_{\mathrm{PCM}}}{\varepsilon}\frac{\partial u}{\partial t}+\frac{\rho_{\mathrm{PCM}}}{\varepsilon^{2}}\left(u\frac{\partial u}{\partial x}+v\frac{\partial u}{\partial y}\right)=-\frac{\partial P}{\partial x}+\left(\frac{\partial}{\partial x}\left(\frac{\mu_{\mathrm{PCM}}}{\varepsilon}\frac{\partial u}{\partial x}\right)+\frac{\partial}{\partial y}\left(\frac{\mu_{\mathrm{PCM}}}{\varepsilon}\frac{\partial u}{\partial y}\right)\right) -\frac{\mu_{\mathrm{PCM}}}{\kappa}u-s(T).u \tag{2}$$

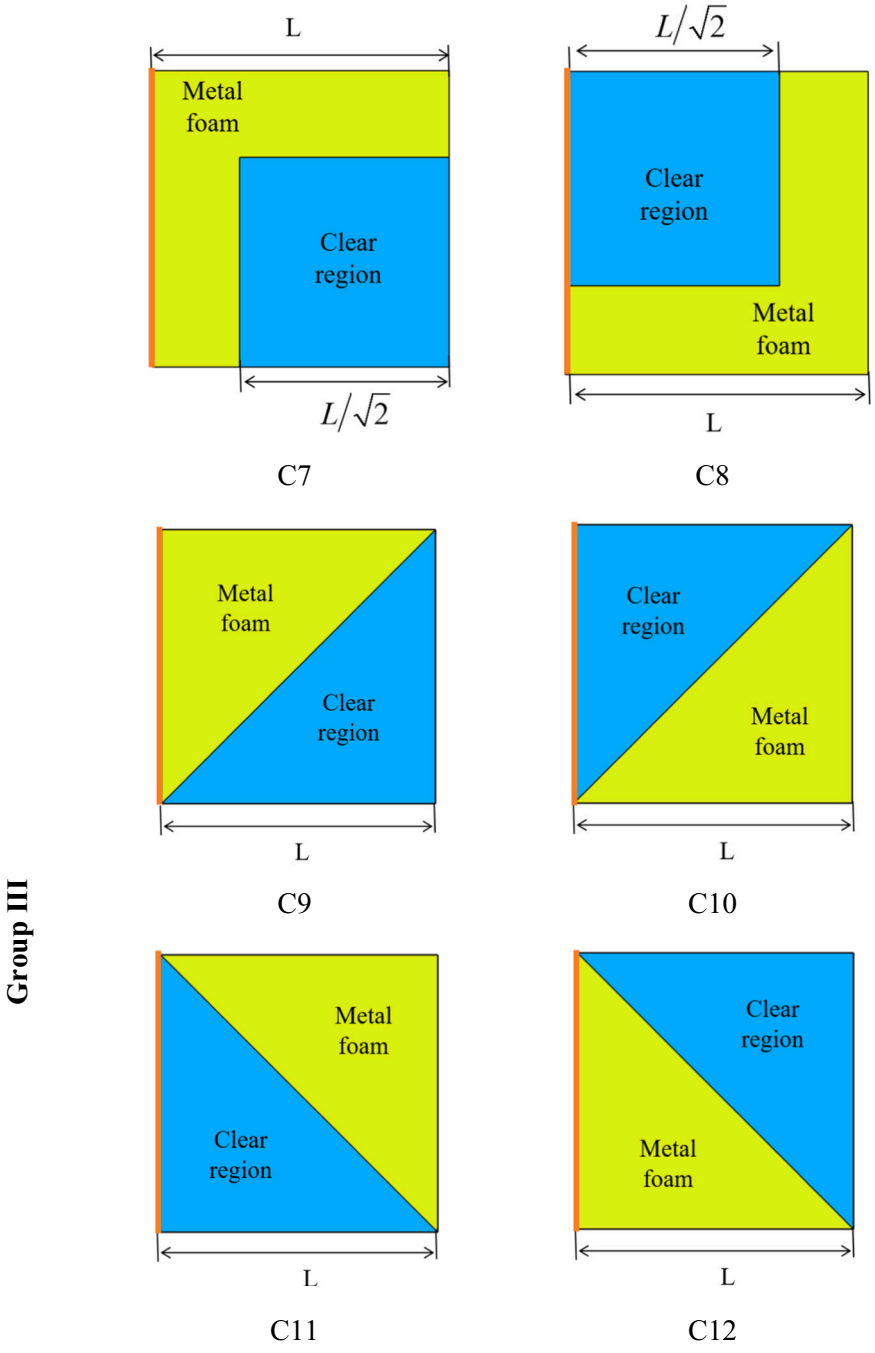

Fig. 2. (*continued*).

$$\frac{\rho_{\mathrm{PCM}}}{\varepsilon}\frac{\partial v}{\partial t}+\frac{\rho_{\mathrm{PCM}}}{\varepsilon^2}\left(u\frac{\partial v}{\partial x}+v\frac{\partial v}{\partial y}\right)=-\frac{\partial P}{\partial y}+\left(\frac{\partial}{\partial x}\left(\frac{\mu_{\mathrm{PCM}}}{\varepsilon}\frac{\partial v}{\partial x}\right)+\frac{\partial}{\partial y}\left(\frac{\mu_{\mathrm{PCM}}}{\varepsilon}\frac{\partial v}{\partial y}\right)\right) -\frac{\mu_{\mathrm{PCM}}}{\kappa}v-s(T).v+\rho_{\mathrm{PCM}}g\beta_{\mathrm{PCM}}\left(T-T_f\right) \tag{3}$$

Conservation of energy:

$$\left(\rho c_p\right)_{\mathrm{eff}}\frac{\partial T}{\partial t}+\left(\rho c_p\right)_{\mathrm{PCM}}\left(u\frac{\partial T}{\partial x}+v\frac{\partial T}{\partial y}\right)+\varepsilon\rho_{\mathrm{PCM}}L_f\frac{\partial\omega(T)}{\partial t} =\frac{\partial}{\partial x}\left(k_{\mathrm{eff,PCM}}\frac{\partial T}{\partial x}\right)+\frac{\partial}{\partial y}\left(k_{\mathrm{eff,PCM}}\frac{\partial T}{\partial y}\right) \tag{4}$$

In the above equations, u and v are the x-velocity and y-velocity components, respectively. T and ω are the temperature and melting volume fraction fields, respectively. Here $s(T)$ is introduced as $s(T)=A_{mush}\frac{(1-\omega(T))^2}{\lambda+\omega^3(T)}$, in which A_{mush} is a large number, and λ was set to 0.001 in order to prevent division by zero. $S(T)$ is a source term that takes a very large value when the liquid fraction is small ($\omega \approx 0$), and it approaches zero in liquid regions $\omega \approx 1$. Finally, g is the gravitational constant and acts in a downward direction. The subscripts f, eff, PCM, s, and l, indicate the fusion, effective properties of composite PCM, phase change material, solid-state, and liquid state, respectively.

In the above equations, x and y denote the local coordinates while t represents time. The thermophysical properties μ, ρ, k, c_p, L_f, and β are the dynamic viscosity, the density, the thermal conductivity, the sensible specific heat capacity, the latent heat of phase change, and the

volumetric thermal expansion coefficient, respectively. The metal foam is characterized by its porosity (ε) and its permeability (κ). The difference between the region with metal foam and the clear region was distinguished by considering the following functions:

$$\text{Clear region}: \begin{cases} \varepsilon \to 1 \\ \kappa \to \infty \end{cases}, \text{metal foam}: \begin{cases} \varepsilon \to \varepsilon_{mf} \\ \kappa \to \kappa_{mf} \end{cases} \tag{5}$$

where the subscript (mf) represents metal foam. Here, the liquid fraction (ω) is introduced based on the temperature around the fusion temperature (T_f):

$$\omega(T) = \begin{cases} 0 & T < T_f - \Delta T_f/2 \\ \dfrac{T - T_f}{\Delta T_f} + \dfrac{1}{2}T_f - \Delta T_f \Big/ 2 & 2 < T < T_f + \Delta T_f \Big/ 2 \\ 1 & T > T_f + \Delta T_f/2 \end{cases} \tag{6}$$

where ΔT_f is the melting temperature range which was adopted as 5 °C. The effective heat capacity and thermal conductivity of PCM in the mushy region were computed as a weighted average of solid and liquid phases:

$$(\rho C_p)_{\text{eff,PCM}} = \phi(\rho C_p)_{\text{eff,PCM,l}} + (1-\phi)(\rho C_p)_{\text{eff,PCM,s}} \tag{7a}$$

$$k_{\text{eff}} = \phi k_{\text{eff,l}} + (1-\phi) k_{\text{eff,s}} \tag{7b}$$

Then, the effective heat capacity and thermal conductivity of composite PCM-metal foam are evaluated using the following equations.

The effective sensible heat capacity of composite-PCM:

$$(\rho C_p)_{\text{eff,PCM,l(s)}} = \varepsilon(\rho C_p)_{\text{PCM,l(s)}} + (1-\varepsilon)(\rho C_p)_{\text{mf}} \tag{8a}$$

The effective density of composite-PCM:

$$\rho_{\text{eff,PCM,l(s)}} = \varepsilon \rho_{\text{PCM,l(s)}} + (1-\varepsilon)\rho_{\text{mf}} \tag{8b}$$

There are several models for computing the effective thermal conductivity of high porosity metal foams, such as [43–45]. The effective thermal conductivity of composite and PCM was computed using the relation proposed by [45], which is in good agreement with the experimental measurements of [46]:

$$k_{\text{eff}} = A\left(\varepsilon k_{PCM} + (1-\varepsilon)k_{mf}\right) + \frac{1-A}{\left(\frac{\varepsilon}{k_{pcm}} + \frac{1-\varepsilon}{k_{mf}}\right)} \tag{8c}$$

where A = 0.35 [45]. The present formulation assumed that there is a local thermal equilibrium between the metal foam and PCM inside the pores. The natural convection was also taken into account using the Boussinesq approximation. Moreover, the density changes during the phase change were also neglected. The large value of A_{mush} was adopted as 1×10^6 in the clear region and 1×10^{10} in the metal foam region. The value of A_{mush} was increased in the metal foam layer since the flow resistance is high in such a region and demands a larger value of A_{mush}. There are excellent relations in literature for computing the permeability of metal foams, such as [47,48]. The pore per inch, ω_p, for metal foam was taken as $\omega_p = 20$ in the present research, and the MF permeability was computed as $\kappa = 2.9764 \times 10^{-7}$ m^2 [48] when $\varepsilon = 0.9$. Moreover, the thermophysical properties of the PCM and the porous matrix are reported in Table 1.

Table 1
Thermophysical properties of paraffin wax and copper [49].

Properties	Paraffin Wax	Copper foam
ρ (kgm^{-3})	900	8900
μ_l (Nsm^{-2})	0.0324	–
C_p (JkgK^{-1})	2300	386
k (Wm^{-1} K^{-1})	0.3	380
h_f (kJkg^{-1})	148.8	–

2.2.2. Controlling boundary and initial conditions

The no-slip boundary condition and Dritchlet thermal boundary condition were applied at the heated wall as:

$$\text{The left heated wall}: u = v = 0 \text{ and } T = T_h \tag{9a}$$

The no-slip and zero heat flux on the other walls:

$$\text{Left, top and bottom walls}: u = v = 0 \text{ and } \frac{\partial T}{\partial n} = 0 \tag{9b}$$

where n is normal to the surface.

Initially, the PCM inside the enclosure is super cold, and the velocity and pressure in the enclosure are zero. Thus, the initial conditions can be introduced as:

$$u = v = 0, P = 0, \text{ and } T = T_{initial} \ @t = 0 \tag{9c}$$

The top left corner of the enclosure was adopted as the reference pressure point with zero-gauge pressure. In the current research, $T_{\text{initial}} = T_f$-10 °C, $T_h = T_f + 10$ °C, and the enclosure size (L) is 50 mm.

2.2.3. The total energy stored in the unit (ES) and melting volume fraction (MVF)

The thermal stored energy in the enclosure is a combination of sensible and latent heat. Thus, the thermal energy storage was computed by integration over the domain from the initial temperature to the current state of the domain as:

$$ES(t) = \overbrace{\int_A \int_{T_{initial}}^{T} (\rho C_p)_{\text{eff,PCM}} dT dA}^{Sensible\ Stored\ Energy} + \overbrace{\varepsilon \int_A \rho_{PCM} \omega h_f dA}^{Latent\ Stored\ Energy} \tag{10}$$

The normal melting volume fraction (NMVF) is evaluated by dividing the volume of liquid PCM to the overall volume of void space in the enclosure as:

$$NMVF = \frac{\int_A \varepsilon\, \omega\, dA}{\int_A \varepsilon\, dA} \tag{11}$$

Finally, the average Nusselt number at the heated surface was introduced using the temperature gradient as:

$$Nu = \frac{k_{eff,PCM} L}{k_{PCM}(T_h - T_f)} \int_0^L \frac{\partial T}{\partial x}\, dy \tag{12}$$

3. Numerical method and validation

This section addresses the numerical method, the mesh sensitivity, and the comparison of the results with the literature studies.

3.1. Numerical method

The finite element method was employed to solve the governing equations for mass, momentum, and energy conservation. The governing equations were first transformed into a weak formulation and then integrated over the physical domain. A schematic view of the solution diagram is depicted in Fig. 3. A Backward Differential Formulation (BDF) was applied to control the time steps and keep the relative solution accuracy below 10^{-4}. The heat and momentum equations were solved fully coupled by the Newton method. The numerical approach is well explained in [50].

3.2. Mesh study

Before the validation of the numerical method, a mesh sensitivity study was first examined. For this purpose, four different computational mesh sizes were tested for an arbitrary case (C5). The melting fraction and the stored energy were investigated for the full melting process, and

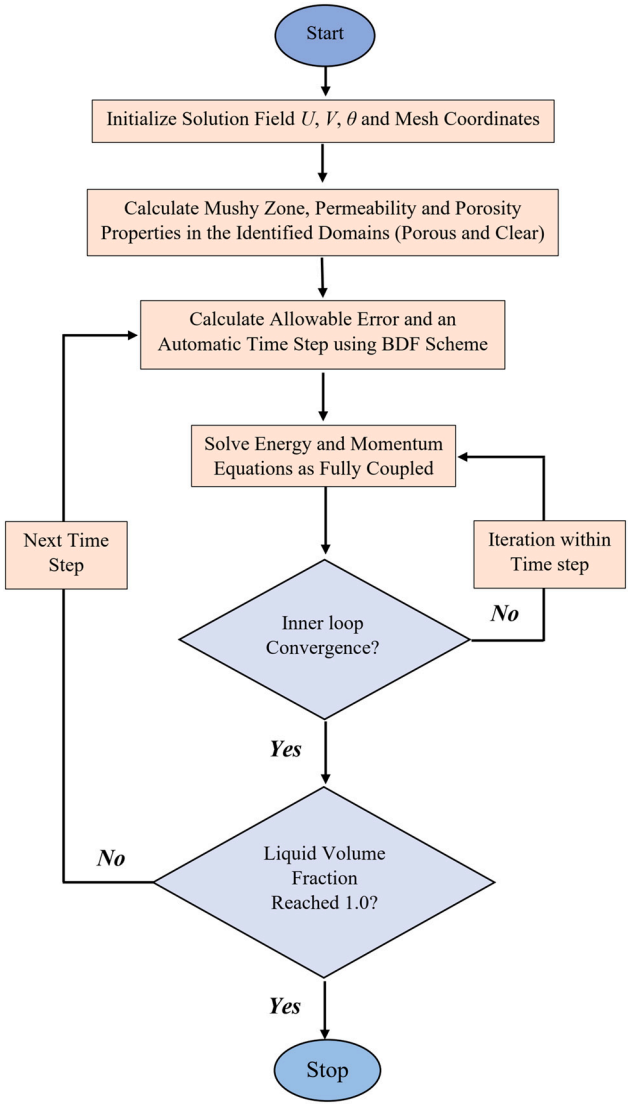

Fig. 3. Diagram of the solution method.

the results are illustrated in Fig. 4. It should be noticed that the effect of changing the geometry, in other words, taking into account other cases, had little effect on the process of assessing the independence of the results from the mesh size. Therefore, the review of the mesh effect on the computation accuracy for the C5 could provide a general estimation of the computational precision.

Details of selected meshes and computed values of the MVF and the total stored energy (TSE) are provided in Table 2. According to the results obtained in Fig. 4, as the size of the mesh elements is reduced, no noticeable difference is observed. Therefore, it can be seen that the results are largely independent of the mesh size. As a compromise between the computational cost and the accuracy, Nmesh = 0.5 was adopted for the rest of the computations. Fig. 5 illustrates a view of the selected mesh for C5, the meshing is quite fine, and mesh elements are square in shape.

3.3. Validation

In this part, the current model results are compared to the literature to guarantee the simulations' correctness and accuracy. As the first comparison, the results of the current study are compared with those of Kamkari and Amlashi [51] and Kamkari et al. [52] for melting a lauric acid in a rectangular enclosure with a vertical heated wall ($T_h = 70\ °C$). The width and heights of the enclosure were 50 mm and 120 mm, respectively. In [51], a local thermal equilibrium model was used. The results for the MVF and the thermal stored energy (TSE) are depicted in Fig. 6. As seen, an acceptable agreement between the computations of the current study and the experimental and numerical literature works can be noticed.

Regarding the melting of composite paraffin wax metal foam, the results of the present code were compared with the experimental data reported by Zheng et al. [49]. The melting of paraffin wax occurred in a square enclosure of size 100 mm, where one of the vertical walls was

Table 2
The characteristics of utilized mesh size for mesh study.

Nmesh	Quad elements	MVF @810 s	TES (kJ) @810 s	Computational time
0.25	62,000	0.956	487	26 h 12 min
0.5	15,625	0.949	482	5 h 28 min
0.75	7026	0.953	484	2 h 42 min
1.0	3949	0.970	494	1 h 32 min

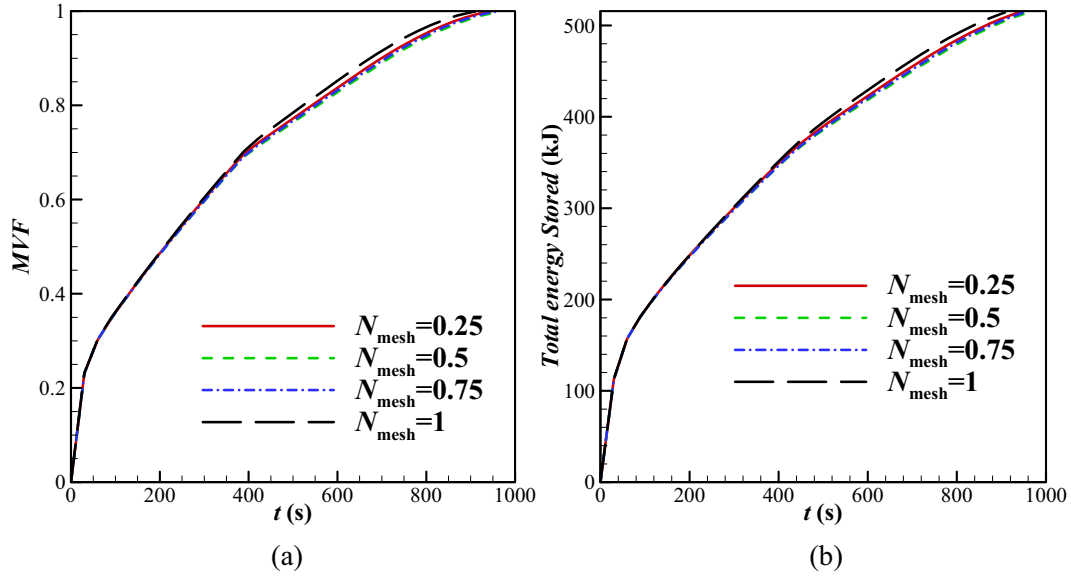

Fig. 4. Evaluation of mesh independency for (a) melting volume fraction, (b) Total energy stored.

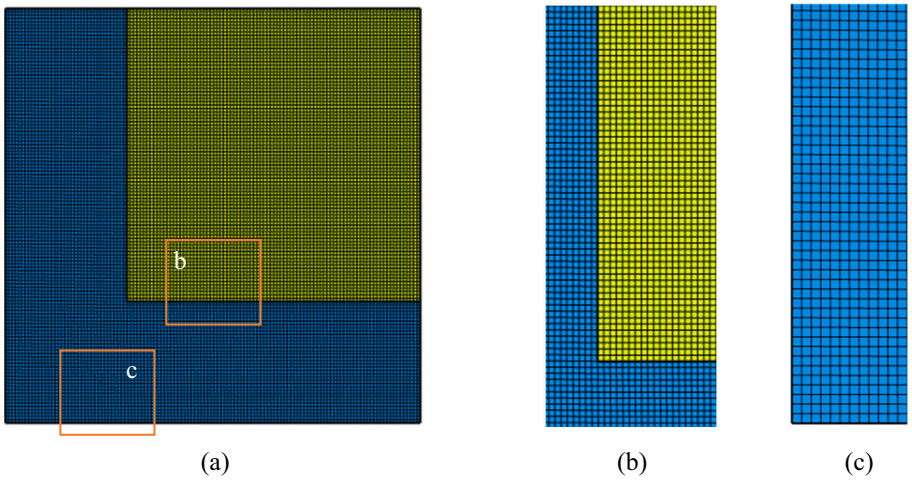

Fig. 5. A view of the selected mesh for C5 with Nmesh = 0.5.

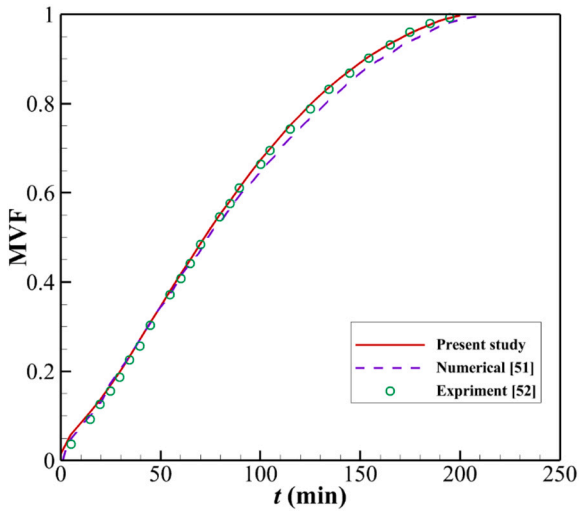

Fig. 6. A comparison between the present study and literature works for MVF as a function of time for the numerical simulations [51] and experimental measurements [52].

heated subject to a constant heat flux (1150 W). There was a slight heat loss from the enclosure sides. The porosity of the copper metal foam was 0.95 and $\omega_p = 5$ PPI. Fig. 7 shows the melting interface at 1.5, 3, and 4.5 h of heating. The shape and the interface locations obtained by the current simulation are very close to those observed by Zheng et al. [49].

4. Results and discussions

In this part, the results for the 12 cases are evaluated. These12 cases are divided into three separate groups (Fig. 2). The first group will involve the placement of the foam layer horizontally (on the bottom and the top) and vertically (on the left and the right), and it includes cases 1 to 4. The second group consists of cases 5 to 8, in which the boundary of the foam layer is separated from a clear quadrilateral medium inside the enclosure. The third group is related to the placement of the foam layer diagonally inside the enclosure, in which cases 9 to 12 are considered.

4.1. Horizontal and vertical foam layer arrangement (cases 1–4)

Fig. 8 shows the melting fraction, the amount of stored energy, and the average Nusselt number inside the enclosure to investigate the first group. Cases 1 and 2 are provided to locate the foam layer in the vertical arrangement. In the first case, the foam layer is adjacent to the warm vertical wall on the left side of the cavity (the active wall), while in the second case, the clear region is adjacent to the right wall (the adiabatic wall). Fig. 8 shows that, in the first case, the melting process is completed faster than in the second case. When the foam layer is adjacent to the hot wall, the melting of the phase change material will be faster than when the clear region occupies the half-enclosure adjacent to the adiabatic wall. Hence, when the foam layer is adjacent to the hot vertical wall, due to the porous solid matrix, the thermal conductivity is increased, and the PCM advances quickly as long as it is in the foam region. A fracture in the middle of the curves indicates the exit or entry of the PCM melting interface from the metal foam into the clear region. When the slope of the curve decreases, the phase-changing material leaves the foam layer and is transferred to the clear region.

On the contrary, the PCM reaches the foam layer from the clear region when the curve slope increases. The clear region has a lower thermal conductivity than the metal foam, so melting the phase change material progresses slowly in a clear region than in a foam layer. In this portion of the curve, a transition from the conduction-dominant mode to the convection-dominant mode can be expected. According to the curve obtained for the first case, the melting volume fraction raised to 50 % with a steep slope. Then, the slope decreases, which shows that the melting interface entered the clear region on the right. At this point, $t =$ 100 s, a fracture occurred in the curve, i.e., the melting interface enters the clear region, and the melting process continues at a lower speed. On the other hand, according to the curve of the second case, a steep slope occurred after the 40 % melting of the PCM. So considering that the porous and clear regions each occupy half of the enclosure, it can be concluded that the melting interface enters the foam layer before it covers the entire clear region. As mentioned, the rate of advance of the melting interface within the foam layer is faster than in the clear region.

Due to natural convection, the advance of the melting interface in the top half of the enclosure is always greater than in the bottom half. Thus, there is a convection-dominant mode at the top region. Nevertheless, using a foam layer can promote the thermal conductivity of the bottom half and promote the conduction heat transfer mechanism.

Cases 3 and 4 show the horizontal arrangement for the foam layer and clear regions. In the third case, the metal foam occupies the bottom half of the enclosure and is at the top half of the enclosure in the fourth case. As it turns out, of all four cases, the shortest time to complete the melting process is in the third case, where about 70 % of the melting process is completed, and then the slope is slightly reduced. In this configuration, when the clear region is in the top half of the enclosure, the melting is boosted by natural convection. Enhancing thermal conductivity by including the foam structure in the bottom will increase the

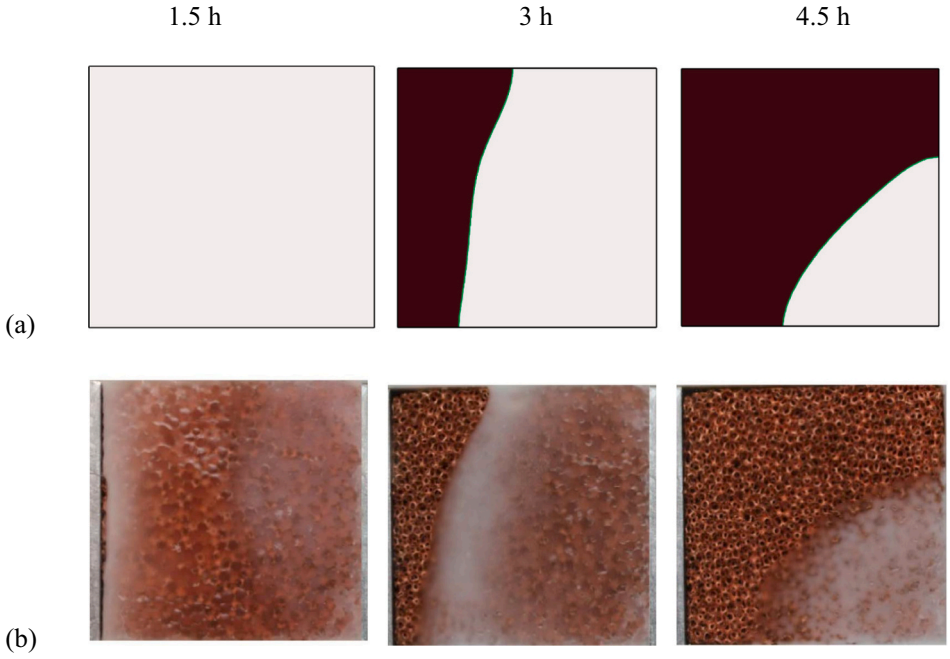

Fig. 7. Melting of composite paraffin wax-copper foam in a square enclosure: (a) the results of the present study and (b) the experimental observation [49].

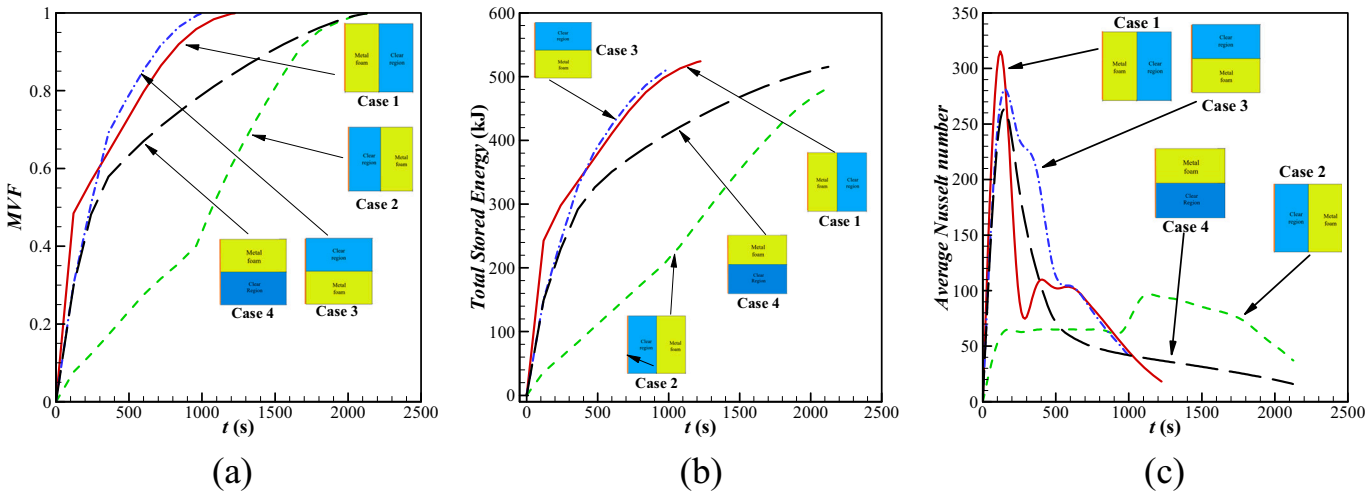

Fig. 8. (a) Melting volume fraction, (b) Total energy stored and (c) Average Nusselt number for group I.

melting rate again. On the contrary, when the foam layer is in the top half of the enclosure (C4), the melting interface advances pretty quickly in the top half. However, it advances slowly at the bottom due to poor effective thermal conductivity and poor convection heat transfer at the bottom area.

The total energy stored for cases 1 to 4 is shown in Fig. 8(b). The patterns obtained for all four cases correspond to the curves in Fig. 8(a). The amount of energy stored for the four curves is roughly equal, except for the third case, where the storage process is fast. It should be noted that the amount of energy stored is also a function of simple and porous media. As can be seen, the amount of energy stored in a foam layer is always greater than in a clear region.

Fig. 8(c) shows the mean Nusselt number adjacent to the left warm wall for cases 1 to 4. According to the obtained results, the highest heat transfer rates for cases 1, 3, and 4 occurred in the very first moments. In contrast, the highest Nusselt number occurred for the second case after the time $t = 1000$s, where the phase change material is entered in the foam layer. For these three cases, in the initial moments, the presence of a phasing material and a cold porous solid matrix next to the hot wall created the highest heat transfer rate. When the foam layer is uniformly adjacent to the hot wall (i.e., C1), the high thermal conductivity of the solid matrix affects the entire thermal boundary layer created adjacent to the hot wall, resulting in the highest heat transfer rate.

The high thermal conductivity of the metal foam composite accelerates the heat transfer between the PCM and the heated wall. The resulting pattern for the first case also weakly occurred for the third and fourth cases. As can be seen, the lower and top half of the enclosure for the third and fourth cases are composed of porous media, respectively. In general, according to the considered boundary conditions, more intense thermal gradients always occur in the lower areas of the left warm wall than in the top areas. Therefore, the placement of a foam layer with high thermal conductivity in the lower half of the enclosure had a greater effect on the average Nusselt number than its placement in the top half of the enclosure. As mentioned, the pattern of the second

case is different from the other three cases. The second case is the only case where the foam layer is not adjacent to the hot wall.

The pure phase change material is initially adjacent to the hot wall. Since its thermal conductivity is lower than the effective thermal conductivity (foam layer relative to the pure material), the heat transfer rate in the early times for the second case is slightly less than in the three other cases. When the molten phase change material reaches the foam layer in the right half of the enclosure, the thermal conductivity is improved, and the circulating melt phase change material is out of thermal equilibrium more than the initial moments. Observing the curves obtained at the last moment makes it possible to get the cases with the highest and lowest heat transfer rates in the first moment and the highest and lowest heat balance in the last moment, respectively. Therefore, increasing the thermal conductivity in the vicinity of the hot wall creates a greater thermal balance at the last moment.

Fig. 9 shows isotherm lines for cases 1 to 4 in the three default times 200 s, 600 s, and 1200s. For this purpose, the temperature range of 326 K to 356 K is considered for all the cases and the three times. Also, the boundary between the foam layer and the clear region is separated by a thick black line to better reflect the changing patterns in these environments. As can be seen, placing the foam layer in the left half of the enclosure (C1) makes the isotherms noticeably wider than in the right half (C2). A closer look at the isotherm shapes in the first row (C1) reveals that the melting interface exits the foam layer on the left and enters the clear region on the right. The isotherms are quite compact around the melting interface in the clear region since the effective thermal conductivity is low. A similar trend for C3 and C4 can be seen when the melting interface is in a clear region.

The set of Fig. 10 shows the streamlines and the forward pattern of the melting interface in the three default times for cases 1 to 4. The obtained patterns are in agreement with the results in Figs. 8 and 9. The streamlines' expansion and the melting interface's progress in cases 1 and 3 are more advanced than in cases 2 and 4. The first and third cases are almost completely melted, $t = 1200$s, a lower melting fraction is observed in case C4, but no significant amount of PCM was melted in case 2.

The streamlines become compact near the melting interface when the meting interface enters a clear region since there is less resistance to flow movement in a clear region. Next to the melting interface, the velocity reaches the natural convection velocity from zero in the solid region, and hence, a notable velocity gradient (compact pattern of streamlines) could be expected. These observations agree with the slope

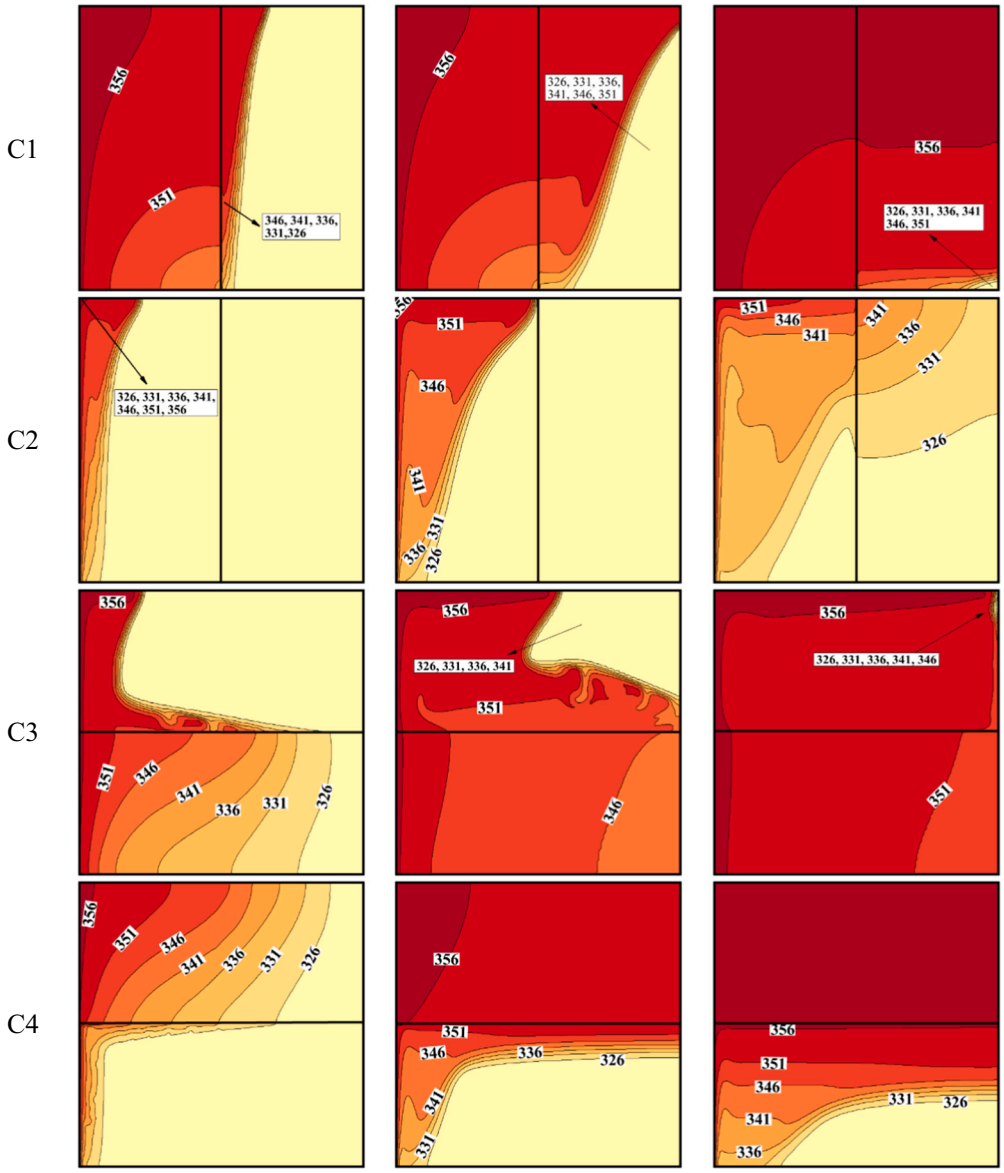

Fig. 9. Variation of contours of isotherm for Group I.

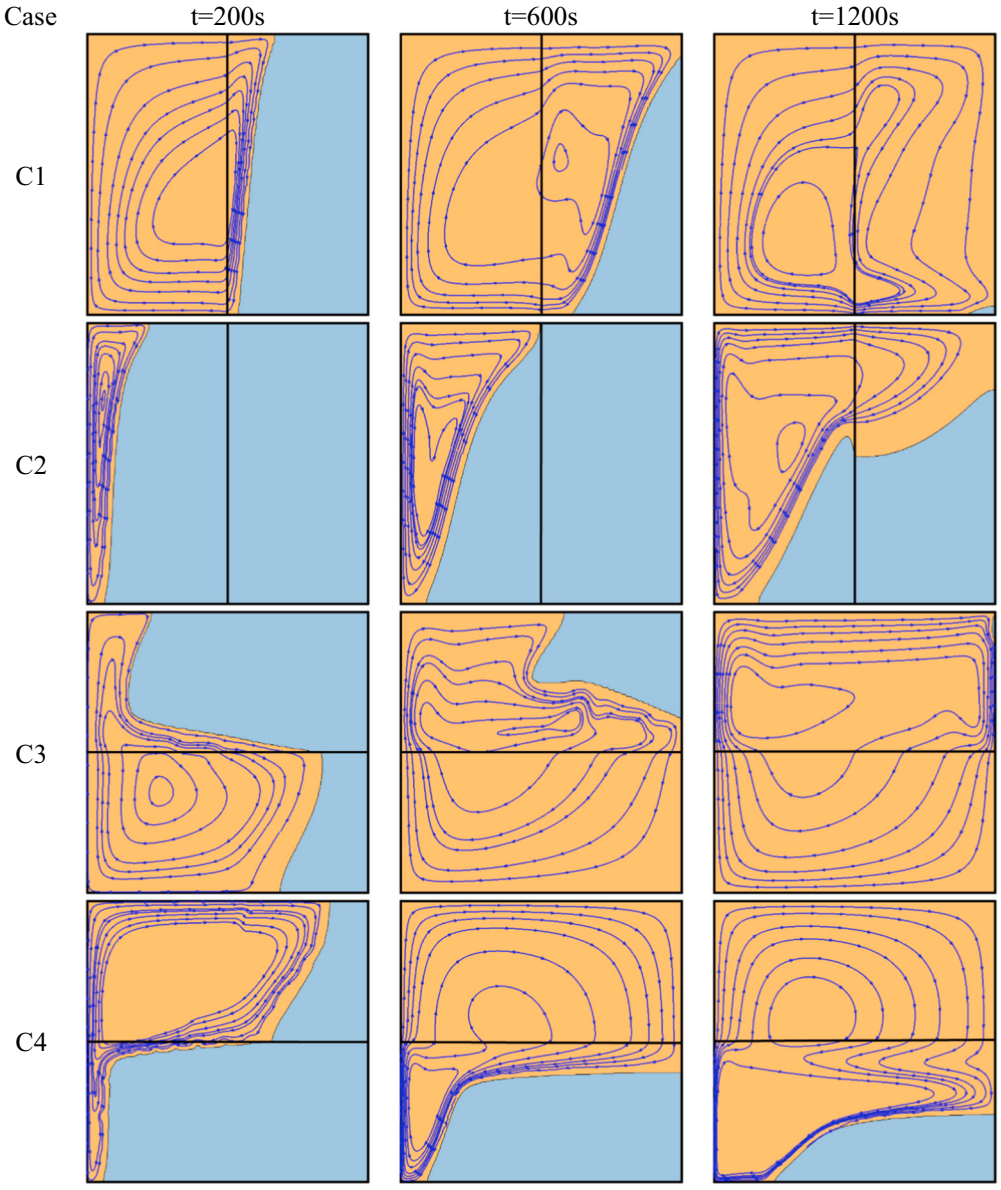

Fig. 10. Variation of streamlines for Group I.

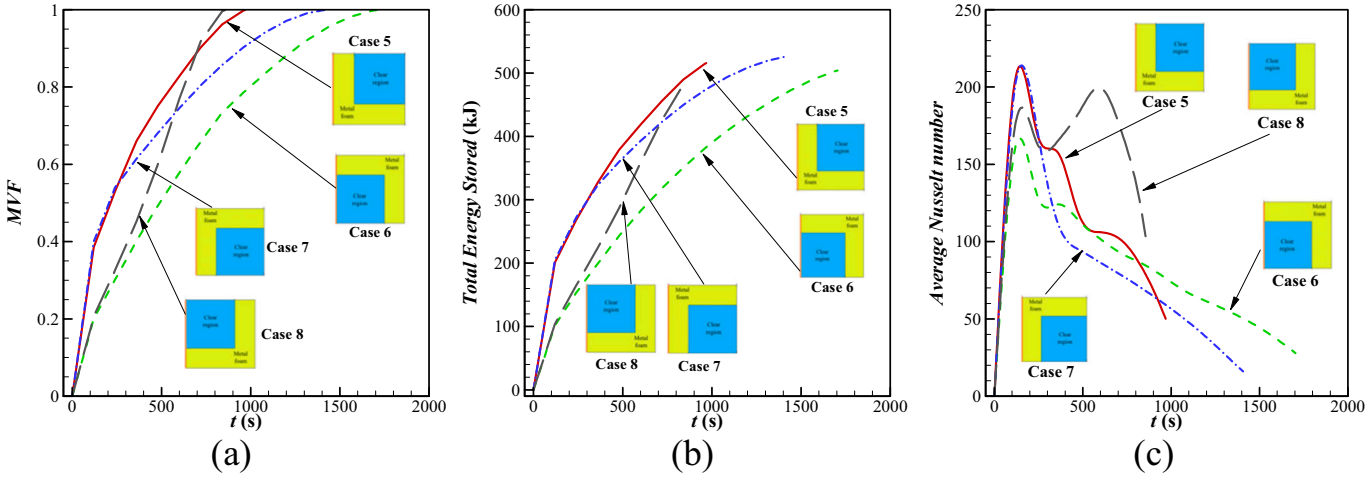

Fig. 11. (a) Melting volume fraction, (b) Total energy stored, and (c) Average Nusselt number for group II.

change in the curve plotted in Fig. 8(a) and the compaction of isotherms in Fig. 9.

4.2. Simple square foam layer arrangement (Cases 5–8)

The arrangement of the second group and its effect on the melting fraction, stored energy, and average Nusselt number is shown in Fig. 11. As mentioned earlier, the simple square environment is located in four different areas of the enclosure, and other than that, the porous solid matrix is placed in the rest of the area. According to Fig. 11(a), C8 is fully melted in the shortest time ($t = 855$ s), and C6 takes the longest time ($t =$ 1704s). Comparing cases 5 and 8 shows that both cases are in contact with the foam layer in the lower parts of the enclosure. In most moments of the melting process, C5 was more advanced than C8, but in the end, the melting process of C8 was completed earlier than C5.

In C5, the foam layer covers the bottom and left areas of the enclosure next to the left wall. This will speed up the melting process until a high amount of PCM melts down. However, a full melting takes a long time since the remaining solid PCM is located in a clear region at the far right of the enclosure. Therefore, according to the observations related to the first group, it can be concluded that advancing the melting interface in the mentioned region at the final stages of thermal charging (melting process) is difficult.

On the other hand, according to the arrangement of C8, more time will be needed to overcome the clear region, but as the melting interface reaches the foam layer, the melting process in the eighth case will be completed faster than in C5. The completion of the melting process for C7 was very similar to C5 until a melting fraction of about 60 % was reached, while after passing the said fraction, the slope of the MVF curve decreased, and more time was needed for the total melting than C5 and C8. Hence, to complete the melting in C7, more time is needed to overcome the clear region of low thermal conductivity at the lower-right areas of the enclosure. The three cases described so far, C5, C7, and C8 had a foam layer area at the bottom of the enclosure adjacent to the hot wall. For C6, with no foam layer at the bottom, the advancement of the melting interface is slow because the thermal conductivity in the remaining regions is poor, and hence, the slope of the MVF reduces.

Following the patterns obtained for the MVF for all four cases in Fig. 11(a), the patterns of the amount of energy stored are shown in Fig. 11(b). As can be seen, a change in the arrangement of the foam /

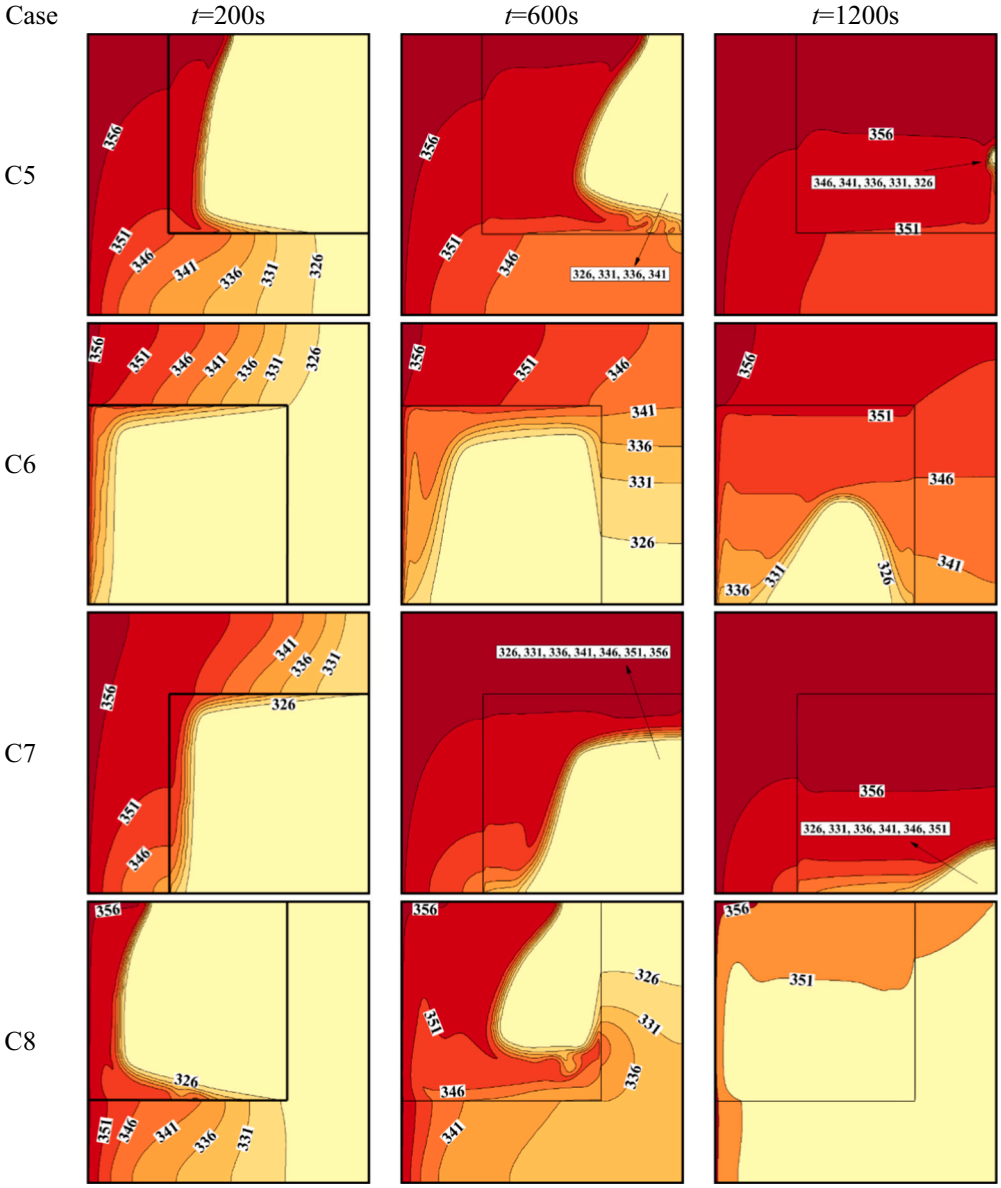

Fig. 12. Variation of contours of isotherm for Group II.

plain medium does not significantly affect the final amount of stored energy. Therefore, only the storage duration is affected.

The average Nusselt number for the C5 to C8 in the predefined time range is shown in Fig. 11(c). As it turns out, when the foam layer is completely adjacent to the hot wall (C5 and C7), the thermal conductivity in those areas increases, and the heat transfer rate for both cases is equally improved. As time progresses, differences between the curves of C5 and C7 can be observed. In C5, the heat transfer rate is gradually reduced, while in the seventh case, the heat transfer rate is suddenly reduced. In the fifth case, the foam layer covers most of the lower half of the enclosure, while in the seventh case, the foam layer covers the top half of the enclosure. Therefore, the arrangement of the foam layer in the fifth case has caused the heat transfer rate to decrease gradually.

The lowest rate of heat transfer in the initial moments belongs to C6 since the clear region is located in the bottom areas of the enclosure. However, after a while, the melting interface reaches the foam layer, and the heat transfer rate increases compare to other cases. Interestingly, the average Nusselt number reached a maximum value at later times for C8.

The development of streamlines and the melting interface propagation for C5 to C8 are shown in Fig. 13. In agreement with Fig. 12, in the early period, the development of streamlines and melting interfaces for C5 and C7 is greater than in the other two cases. At $t = 600$ s, not only do C5 and C7 show a good development of the melting interface, but also C8 shows a comparable advancement of the melting interface. At the last time ($t = 1200$s), the melting process is almost completed for C5 and C8. However, some notable regions of C6 and C7 are still solid.

4.3. Diagonal foam layer arrangement (Cases 9–12)

The impact of the diagonal placement of the metal foam layer on the melting behavior is evaluated in the third group for C9 to C12. Fig. 14(a) to (c) show the effect of diagonal arrangement on MVF, the amount of stored energy, and the average Nusselt. In order to better identify the mentioned cases, the term diametric arrangement is used for C9 and C10, and the term opposite diametric arrangement is used for C11 and C12. As shown in Fig. 14(a), C9 and C12 are fully melted in the shortest time, and cases 10 and 11 are fully melted later. The melting process is faster when the foam layer is adjacent to the hot vertical wall regardless of the diametric and opposite diametric arrangements. The difference between C 9 and C12 is in the position of the metal foam layer because

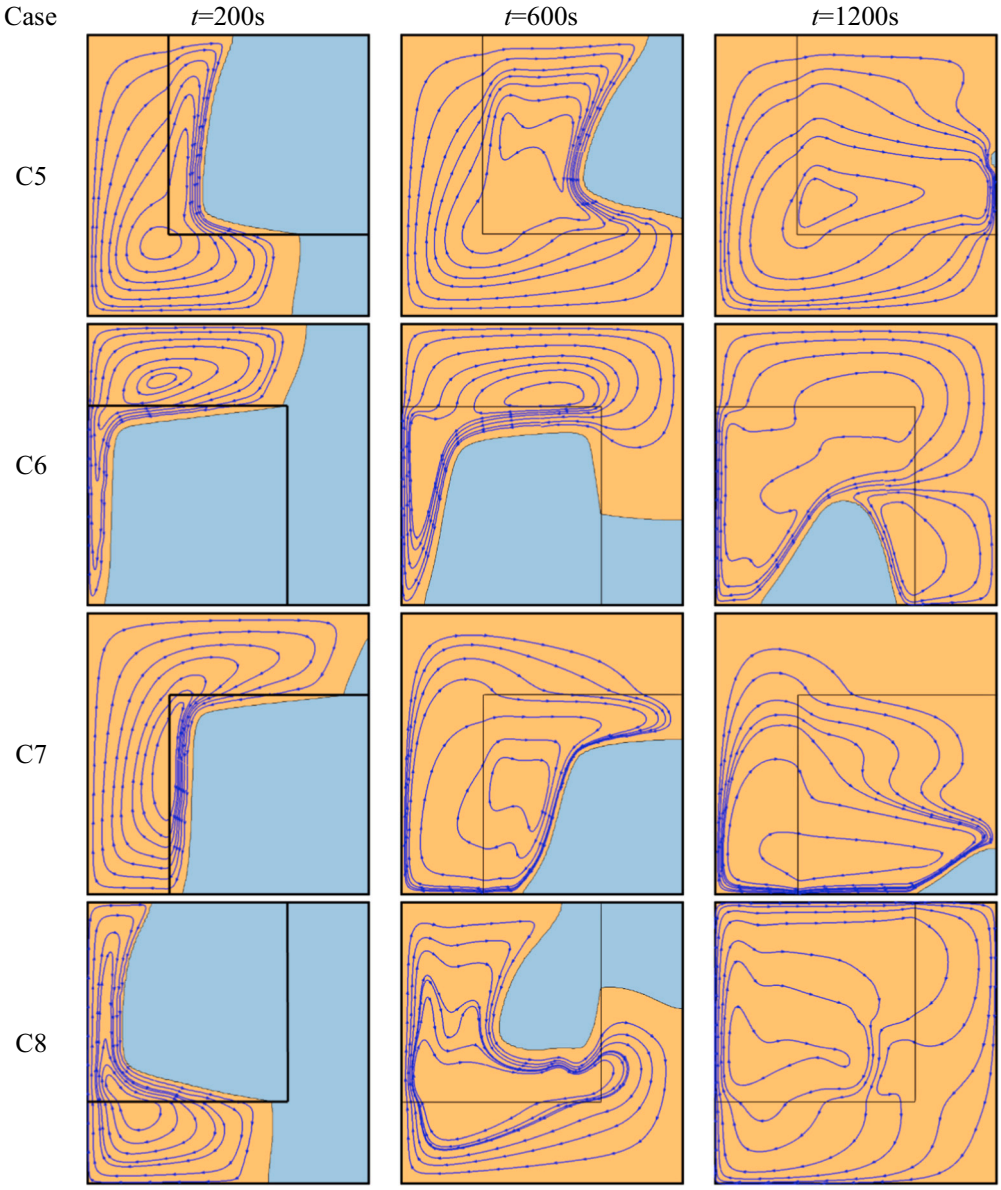

Fig. 13. Variation of contours of isotherm for Group II.

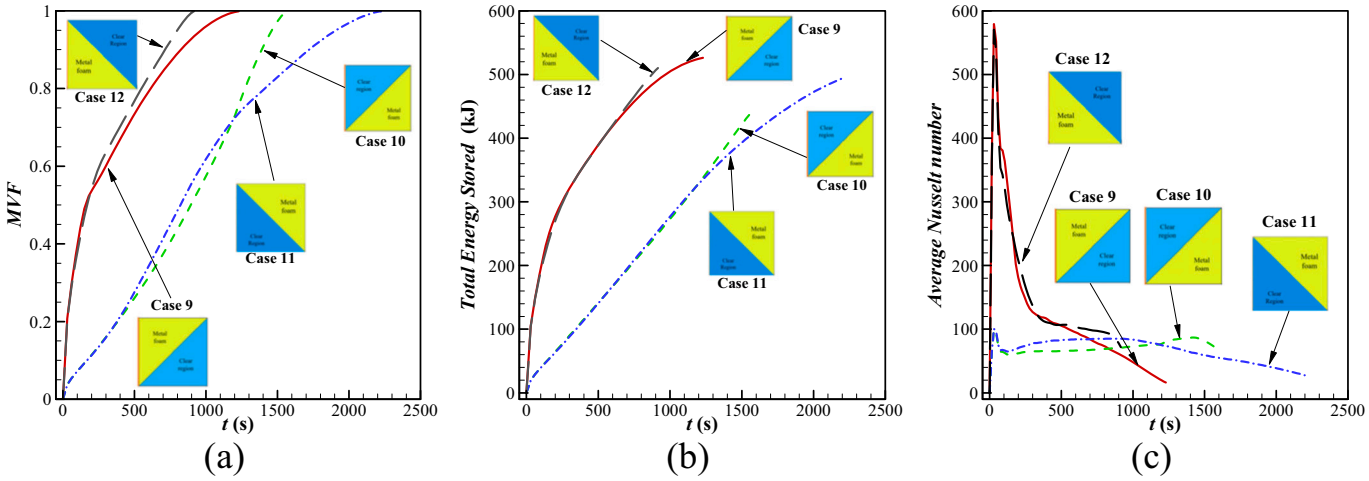

Fig. 14. (a) Melting volume fraction, (b) Total energy stored and (c) Average Nusselt number for group III.

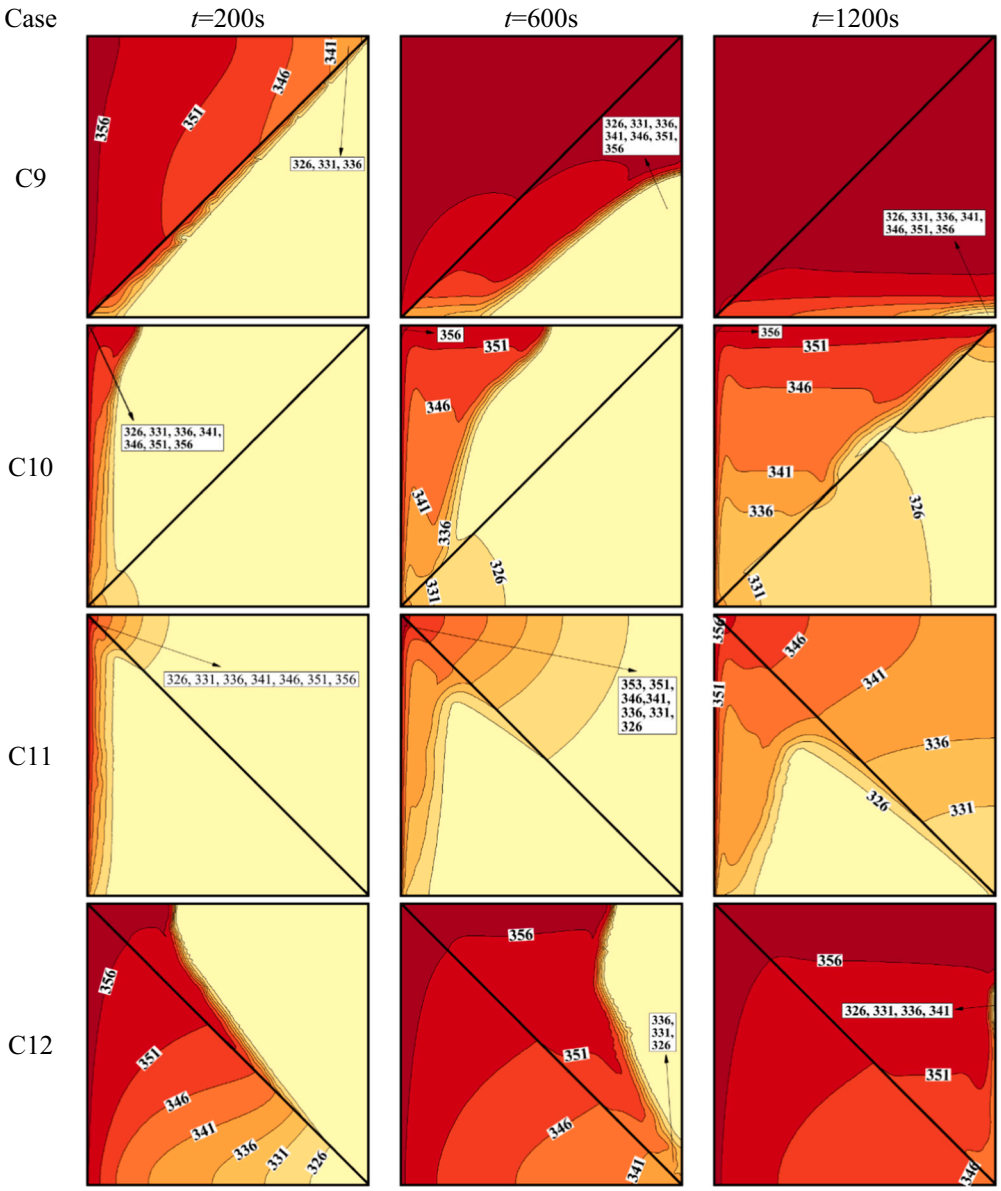

Fig. 15. Variation of contours of isotherm for Group III.

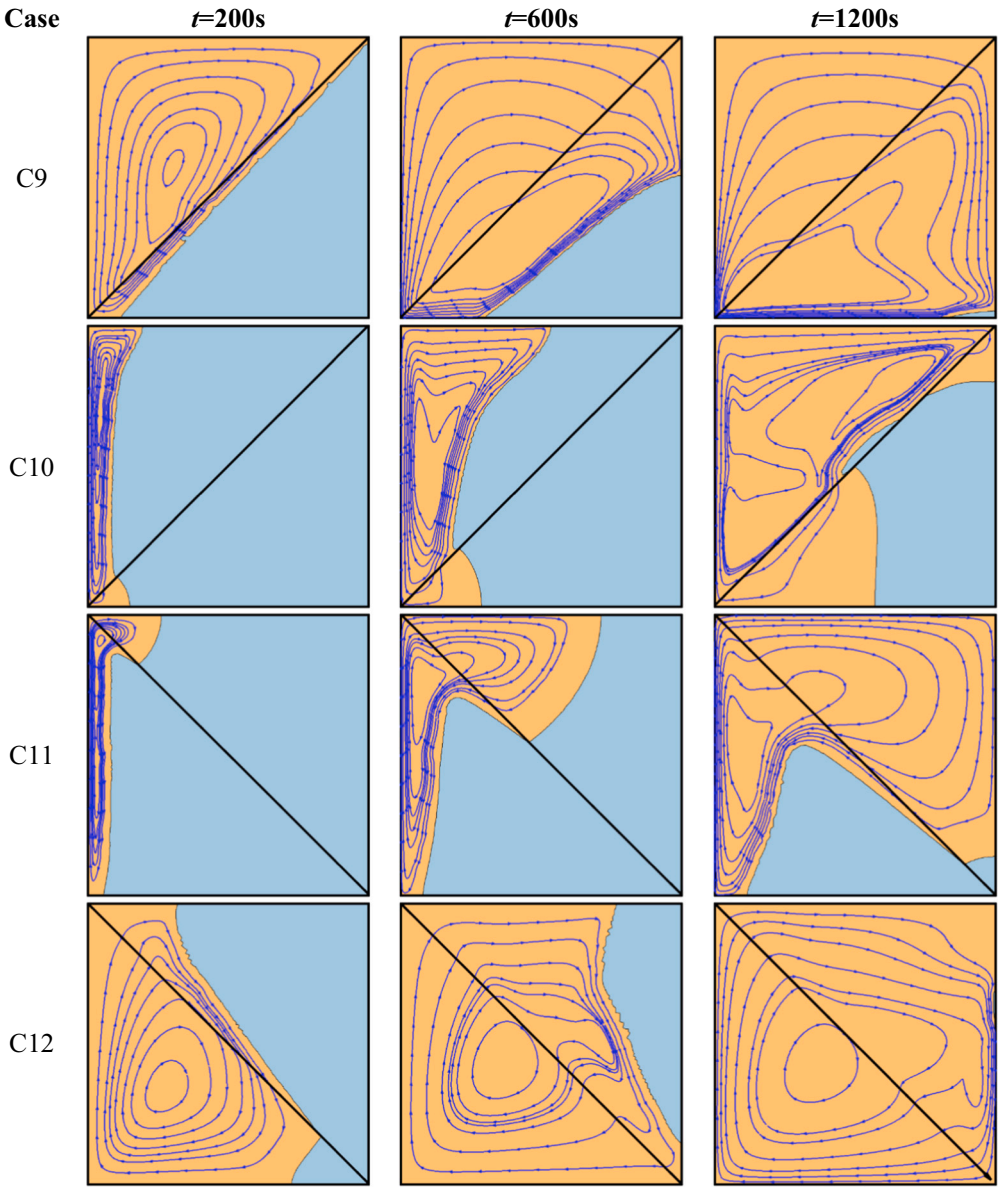

Fig. 16. Variation of streamlines for Group II.

when the foam layer is in the diametric arrangement (C9), it occupies the top areas of the enclosure. When it is in the opposite diametric arrangement (C12), it includes the bottom areas of the enclosure.

Placing the metal foam in the bottom areas accelerates the melting interface's advancement due to the foam layer's high thermal conductivity. Therefore, the melting process in C12 is completed slightly earlier than in C9. The progress of MVF for C10 and C11 up to the melt fraction of 80 % (t = 1200s) is almost the same, while the onset of divergence between the two curves occurred after t = 1200s. As previously described, in a clear region, the advancement of the melting interface at the top regions of the enclosure is much better than bottom regions due to much better natural convection heat transfer at the top. The arrangement of C10 (diametric arrangement) is such that the PCM enters the foam layer from the bottom areas of the enclosure. Therefore, the advancement of the melting interface continues from both the bottom and top regions.

On the other hand, in C11 (opposite diametric arrangement), the advancement of the melting interface is high at the top areas, where it enters the foam layer. However, it remains small from the bottom areas of the enclosure. Therefore, melting of the PCM in the bottom part of C11 takes longer than in C10.

Fig. 14(b) shows the amount of stored energy for C9 to C12. The total stored energy follows similar patterns to the curves in Fig. 14(a). In fact, the faster the melting process, the higher the rate of thermal energy storage. The difference in the amount of stored energy for all four cases at the last time is related to the sensible heat. The latent energy storage reaches its maximum value when the melting process is completed.

The average Nusselt number for Group III is shown in Fig. 14(c). The presence of a foam layer adjacent to the heated wall (C9 and C12) enhances the heat transfer rate. However, the absence of the foam layer near the hot wall (C10 and C11) decreases the heat transfer at initial times.

The isotherms for C9 to C12 are shown in Fig. 15. At any given time, the broadest range of streamlines belongs to C9 and C12 since the foam layer is adjacent to the left wall (active wall). With the entry of the liquid PCM into the clear region, the isotherms become compact, which is due to the low thermal conductivity in the clear region. The opposite behavior of the isotherms can be seen in C10 and C11 (see rows 2 and 3). As long as the isotherms are in a clear region and adjacent to the active wall, a high density of isotherms can be seen, which indicates a high-

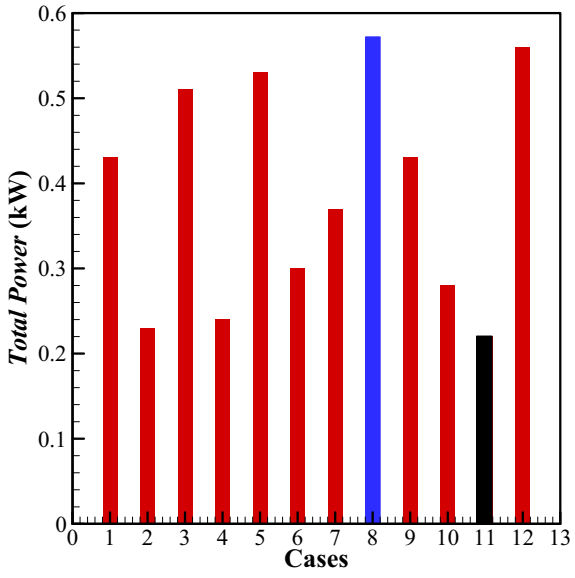

Fig. 17. Total power stored by the cases, (Blue) Maximum power stored via C8, (Black) minimum power stored via C11, and (Reds) The other cases. (For interpretation of the references to colour in this figure legend, the reader is referred to the web version of this article.)

temperature gradient. When these isotherms enter the foam layer, they suddenly expand due to the high thermal conductivity of the composite-PCM. These observations agree with Fig. 14(a) and (c).

Fig. 16 shows the streamlines and melting interface pattern for C9 to C12 in three default times. The expansion of the streamlines and a fair advancement of the melting interface can be observed in C9 and C12 in an early time of $t = 200$ s. Moreover, the melting interface is quite behind in C10 and C11, and the streamlines are pretty compact since they are in a clear flow region. Over time, when the liquid PCM leaves the metal foam layer of C9 and C12, the streamlines and melting interface are compacted. In contrast, the flow and melting interface lines expand dramatically when the liquid PCM enters the foam layer.

4.4. All arrangement comparison

After examining the melting process for the three groups, the energy storage power of each configuration can be computed as the amount of stored energy over the storage time. The energy storage power of the 12 foam layer arrangements is plotted in Fig. 17. It is important to note that the area occupied by the foam layer is the same in all cases, so it makes sense to judge the efficiency of the 12 cases based on the energy storage power. C8 in blue with 0.57 kW and C11 in black with 0.22 kW represent the highest and lowest energy storage power among the investigated configurations. To be more precise, the effect of arranging the foam layer inside the energy storage enclosure for the best case (C8) can be up to 2.6 times greater than the worst-case (C11). After C8, C12 could provide the best energy storage power.

5. Conclusion

The influence of the shape and mounting place of a metal foam layer was addressed in the melting rate and energy storage power of an LHTES unit. The metal foam layer was investigated in three design groups Group I: Straight partition; Group II: Square partition; Group III: Diagonal partition. The time profiles of the total stored energy, MVF, Average Nusselt number, streamlines, and temperature contours were reported for each design group. The main outcomes can be summarized as follows:

(a) For design group I (straight partition), laying the metal foam layer horizontally along the bottom wall (C'3) results in the fastest melting time (~15 min) melting time. The second-best case was laying the foam layer vertically along the heated wall (left wall). These two configurations could allow a fair enhanced conduction heat transfer at the initial melting heat transfer and a fair natural convection circulation at the final stages of melting.

(b) For design group II (square partition), the best case was C8, in which the metal foam layer was placed at the bottom right. In this design, the melting was developed from the bottom of the foam layer and then led to a robust natural convection circulation. This design provides a uniform storage rate along the charging process. Placing the foam layer at the bottom right also produces a good storage power close to C8. However, in this design, the storage rate is very high due to a very good local thermal conductivity enhancement of the foam layer along the heated wall and bottom. However, at the final stages of the charging process, there is no metal foam in the solid PCM, and hence the charging rate drops.

(c) For design group III (diagonal partition), The foam layer should be placed next to the heated wall. Laying the rest of the foam next to the bottom wall gives the best melting rate in this group since it allows a better natural convection circulation at the final stages of the melting process. Placing the foam layer next to the vertical insulated walls delays the PCM melting at the initial thermal charging stages, which generally is not beneficial.

(d) Among all investigated cases, C8, with 15 min charging time, provides the highest melting and thermal energy storage rate (power). In C8, the metal foam layer was laid along the bottom and right walls. This design provides an initial boost in melting heat transfer by enhancing the conduction heat transfer along the bottom wall and then boosts the natural convection heat when 50 % of the enclosure is melted. It also helps the thermal charging be completed quickly at the final melting stage since a foam layer locally supports the remaining solid PCM. C11 was the worst case with about 37 min charging time. In this case, the foam layer is configured diagonally along the right and top walls. This configuration eliminates the benefit of the foam layer at the initial melting stages and suppresses the convection heat transfer at the final melting stages. Placing the foam layer with the configuration C8 leads to 60 better charging power than C11.

CRediT authorship contribution statement

M.A. Fteiti: Conceptualization, Methodology, Software, Validation, Formal analysis, Data Curatio, Original draft preparation, Writing - Review & Editing, Supervision. **M. Ghalambaz:** Visualization, Investigation. Formal analysis, Writing - Review & Editing, Supervision **O. Younis:** Original draft preparation, Investigation, Formal analysis, Writing - Review & Editing. **M. Sheremet:** Methodology, Investigation, Writing - Review & Editing. **M. Ismael:** Methodology, Software; Formal analysis, Data Curation, Investigation, Writing - Review & Editing.

Declaration of competing interest

The authors clarify that there is no conflict of interest for report.

Data availability

No data was used for the research described in the article.

Acknowledgments

The authors would like to thank the Deanship of Scientific Research at Umm Al-Qura University for supporting this work by Grant Code: (22UQU4310414DSR03). This research of Mohammad Ghalambaz and

Mikhail Sheremet was supported by the Tomsk State University Development Programme (Priority-2030).

References

[1] B. Ahmadi, M. Ahmadi, K. Nawaz, A.M. Momen, S. Bigham, Performance analysis and limiting parameters of cross-flow membrane-based liquid-desiccant air dehumidifiers, Int. J. Refrig. 132 (2021) 21–29.

[2] K. Du, J. Calautit, P. Eames, Y. Wu, A state-of-the-art review of the application of phase change materials (PCM) in Mobilized-thermal Energy Storage (M-TES) for recovering low-temperature industrial waste heat (IWH) for distributed heat supply, Renew. Energy 168 (2021) 1040–1057.

[3] M. Dardir, K. Panchabikesan, F. Haghighat, M. El Mankibi, Y. Yuan, Opportunities and challenges of PCM-to-air heat exchangers (PAHXs) for building free cooling applications—a comprehensive review, J.Energy Storage 22 (2019) 157–175.

[4] S. Zhang, D. Feng, L. Shi, L. Wang, Y. Jin, L. Tian, Z. Li, G. Wang, L. Zhao, Y. Yan, A review of phase change heat transfer in shape-stabilized phase change materials (ss-PCMs) based on porous supports for thermal energy storage, Renew. Sust. Energ. Rev. 135 (2021).

[5] R. Chaturvedi, A. Islam, K. Sharma, A review on the applications of PCM in thermal storage of solar energy, Mater.TodayProc. 43 (2021) 293–297.

[6] S. Rostami, M. Afrand, A. Shahsavar, M. Sheikholeslami, R. Kalbasi, S. Aghakhani, M.S. Shadloo, H.F. Oztop, A review of melting and freezing processes of PCM/nano-PCM and their application in energy storage, Energy 211 (2020).

[7] X. Huang, G. Alva, Y. Jia, G. Fang, Morphological characterization and applications of phase change materials in thermal energy storage: a review, Renew. Sust. Energ. Rev. 72 (2017) 128–145.

[8] S. Mishra, P. Mathur, H.M. Ali, Analysis of homogeneous–heterogeneous reactions in a micropolar nanofluid past a nonlinear stretching surface: semi-analytical approach, J. Therm. Anal. Calorim. 144 (2021) 2247–2257.

[9] J. Guo, Z. Liu, B. Yang, X. Yang, J. Yan, Melting assessment on the angled fin design for a novel latent heat thermal energy storage tube, Renew. Energy 183 (2022) 406–422.

[10] X. Yang, X. Wang, Z. Liu, X. Luo, J. Yan, Effect of fin number on the melting phase change in a horizontal finned shell-and-tube thermal energy storage unit, Sol. Energy Mater. Sol. Cells 236 (2022), 111527.

[11] S.U. Khalid, H. Babar, H.M. Ali, M.M. Janjua, M.A. Ali, Heat pipes: progress in thermal performance enhancement for microelectronics, J. Therm. Anal. Calorim. 143 (2021) 2227–2243.

[12] S. Ashraf, M. Sultan, M. Bahrami, C. McCague, M.W. Shahzad, M. Amani, R. R. Shamshiri, H.M. Ali, Recent progress on water vapor adsorption equilibrium by metal-organic frameworks for heat transformation applications, Int.Commun. HeatMass Transf. 124 (2021), 105242.

[13] J. Guo, X. Wang, B. Yang, X. Yang, M.-J. Li, Thermal assessment on solid-liquid energy storage tube packed with non-uniform angled fins, Sol. Energy Mater. Sol. Cells 236 (2022), 111526.

[14] X. Yang, J. Guo, B. Yang, H. Cheng, P. Wei, Y.-L. He, Design of non-uniformly distributed annular fins for a shell-and-tube thermal energy storage unit, Appl. Energy 279 (2020), 115772.

[15] R. Tauseef ur, H.M. Ali, M.M. Janjua, U. Sajjad, W.-M. Yan, A critical review on heat transfer augmentation of phase change materials embedded with porous materials/foams, Int. J. Heat Mass Transf. 135 (2019) 649–673.

[16] C. Yu, Y. Huang, C. Zhang, Role of metal foam in solidification performance for a latent heat storage unit, Int. J. Energy Res. 44 (2019) 2110–2125.

[17] V. Joshi, M.K. Rathod, Thermal performance augmentation of metal foam infused phase change material using a partial filling strategy: an evaluation for fill height ratio and porosity, Appl. Energy 253 (2019).

[18] M. Gaedtke, S. Abishek, R. Mead-Hunter, A.J.C. King, B.J. Mullins, H. Nirschl, M. J. Krause, Total enthalpy-based lattice Boltzmann simulations of melting in paraffin/metal foam composite phase change materials, Int. J. Heat Mass Transf. 155 (2020).

[19] H.M. Ali, Heat transfer augmentation of porous media (metallic foam) and phase change material based heat sink with variable heat generations: an experimental evaluation, Sustain.Energy Technol.Assess. 52 (2022), 102218.

[20] Z. Li, A. Shahsavar, A.A.A.A. Al-Rashed, P. Talebizadehsardari, Effect of porous medium and nanoparticles presences in a counter-current triple-tube composite porous/nano-PCM system, Appl. Therm. Eng. 167 (2020).

[21] X. Meng, L. Yan, J. Xu, F. He, H. Yu, M. Zhang, Effect of porosity and pore density of copper foam on thermal performance of the paraffin-copper foam composite phase-change material, Case Stud.Therm.Eng. 22 (2020).

[22] J. Guo, Z. Du, G. Liu, X. Yang, M.-J. Li, Compression effect of metal foam on melting phase change in a shell-and-tube unit, Appl. Therm. Eng. 206 (2022), 118124.

[23] Shahriyar Hekmat, G.R. Molaeimanesh, Thermal Management System for Battery Module, 2020. United States.

[24] F.C.Zhang Junsheng, Wang Jian, in: Heat Dissipation Device And Electronic Equipment, 2020.

[25] Z.A. Qureshi, E. Elnajjar, O. Al-Ketan, R.A. Al-Rub, S.B. Al-Omari, Heat transfer performance of a finned metal foam-phase change material (FMF-PCM) system incorporating triply periodic minimal surfaces (TPMS), Int. J. Heat Mass Transf. 170 (2021).

[26] Z.A. Qureshi, S.A.B. Al-Omari, E. Elnajjar, O. Al-Ketan, R.A. Al-Rub, Using triply periodic minimal surfaces (TPMS)-based metal foams structures as skeleton for metal-foam-PCM composites for thermal energy storage and energy management applications, Int.Commun.HeatMass Transf. 124 (2021).

[27] N. Bianco, S. Busiello, M. Iasiello, G.M. Mauro, Finned heat sinks with phase change materials and metal foams: pareto optimization to address cost and operation time, Appl. Therm. Eng. 197 (2021).

[28] P.T. Sardari, H.I. Mohammed, D. Giddings, G.S. Walker, M. Gillott, D. Grant, Numerical study of a multiple-segment metal foam-PCM latent heat storage unit: effect of porosity, pore density and location of heat source, Energy 189 (2019).

[29] Z.-Q. Zhu, Y.-K. Huang, N. Hu, Y. Zeng, L.-W. Fan, Transient performance of a PCM-based heat sink with a partially filled metal foam: effects of the filling height ratio, Appl. Therm. Eng. 128 (2018) 966–972.

[30] Y. Xu, Q. Ren, Z.-J. Zheng, Y.-L. He, Evaluation and optimization of melting performance for a latent heat thermal energy storage unit partially filled with porous media, Appl. Energy 193 (2017) 84–95.

[31] Y. Xu, M.-J. Li, Z.-J. Zheng, X.-D. Xue, Melting performance enhancement of phase change material by a limited amount of metal foam: configurational optimization and economic assessment, Appl. Energy 212 (2018) 868–880.

[32] J. Sutradhar, R. Kothari, S.K. Sahu, Melting and solidification analysis of phase change material-metal foam composite with expansion/shrinkage void in rectangular system, J.Energy Storage 47 (2022).

[33] X.K. Yu, Y.B. Tao, Y. He, Z.C. Lv, Temperature control performance of high thermal conductivity metal foam/paraffin composite phase change material: an experimental study, J.Energy Storage 46 (2022).

[34] Y. Zhuang, J. Lin, A. Liu, Numerical investigation on non-Newtonian melting heat transfer of phase change material composited with nanoparticles and metal foam in an inner heated cubic cavity, J.Energy Storage 51 (2022).

[35] C. Naldi, M. Dongellini, G.L. Morini, The evaluation of the effective thermal conductivity of metal-foam loaded phase change materials, J.Energy Storage 51 (2022).

[36] H. Shakibi, S. Afzal, A. Shokri, B. Sobhani, Utilization of a phase change material with metal foam for the performance improvement of the photovoltaic cells, J. Energy Storage 51 (2022).

[37] J.S. Baruah, V. Athawale, P. Rath, A. Bhattacharya, Melting and energy storage characteristics of macro-encapsulated PCM-metal foam system, Int. J. Heat Mass Transf. 182 (2022).

[38] A.A. Nnanna, A. Haji-Sheikh, K.T. Harris, Experimental study of local thermal non-equilibrium phenomena during phase change in porous media, Int. J. Heat Mass Transf. 47 (2004) 4365–4375.

[39] K. Jiao, L. Lu, T. Wen, Q. Wang, A modified mixture theory for one-dimensional melting of pure PCM and PCM/metal foam composite: numerical analysis and experiment validation, Int. J. Heat Mass Transf. 186 (2022), 122461.

[40] X. Hu, X. Gong, Pore-scale numerical simulation of the thermal performance for phase change material embedded in metal foam with cubic periodic cell structure, Appl. Therm. Eng. 151 (2019) 231–239.

[41] J.M. Mahdi, H.I. Mohammed, E.T. Hashim, P. Talebizadehsardari, E.C. Nsofor, Solidification enhancement with multiple PCMs, cascaded metal foam and nanoparticles in the shell-and-tube energy storage system, Appl. Energy 257 (2020), 113993.

[42] S.M.H. Zadeh, S. Mehryan, M. Ghalambaz, M. Ghodrat, J. Young, A. Chamkha, Hybrid thermal performance enhancement of a circular latent heat storage system by utilizing partially filled copper foam and Cu/GO nano-additives, Energy 213 (2020), 118761.

[43] X.H. Yang, J.X. Bai, H.B. Yan, J.J. Kuang, T.J. Lu, T. Kim, An analytical unit cell model for the effective thermal conductivity of high porosity open-cell metal foams, Transp. Porous Media 102 (2014) 403–426.

[44] X. Yang, J. Kuang, T. Lu, F. Han, T. Kim, A simplistic analytical unit cell based model for the effective thermal conductivity of high porosity open-cell metal foams, J. Phys. D. Appl. Phys. 46 (2013), 255302.

[45] A. Bhattacharya, V.V. Calmidi, R.L. Mahajan, Thermophysical properties of high porosity metal foams, Int. J. Heat Mass Transf. 45 (2002) 1017–1031.

[46] X. Xiao, P. Zhang, M. Li, Preparation and thermal characterization of paraffin/metal foam composite phase change material, Appl. Energy 112 (2013) 1357–1366.

[47] X. Yang, T.J. Lu, T. Kim, An analytical model for permeability of isotropic porous media, Phys. Lett. A 378 (2014) 2308–2311.

[48] D.A. Nield, A. Bejan, Convection in Porous Media, Springer, 2006.

[49] H. Zheng, C. Wang, Q. Liu, Z. Tian, X. Fan, Thermal performance of copper foam/paraffin composite phase change material, Energy Convers. Manag. 157 (2018) 372–381.

[50] O.C. Zienkiewicz, R.L. Taylor, P. Nithiarasu, The Finite Element Method for Fluid Dynamics, Seventh Edition ed., Butterworth-Heinemann, Oxford, 2014.

[51] B. Kamkari, H.J. Amlashi, Numerical simulation and experimental verification of constrained melting of phase change material in inclined rectangular enclosures, Int.Commun.HeatMass Transf. 88 (2017) 211–219.

[52] B. Kamkari, H. Shokouhmand, F. Bruno, Experimental investigation of the effect of inclination angle on convection-driven melting of phase change material in a rectangular enclosure, Int. J. Heat Mass Transf. 72 (2014) 186–200.